The differences between remote sensing and in situ air pollutants measurements over the Canadian Oil Sands

Xiaoyi Zhao[1], Vitali Fioletov[1], Debora Griffin[1], Chris McLinden[1], Ralf Staebler[1], Cristian Mihele[1], Kevin Strawbridge[1], Jonathan Davies[1], Ihab Abboud[1], Sum Chi Lee[1], Alexander Cede[2,3], Martin Tiefengraber[3,4], Robert Swap[2]

[1]Air Quality Research Division, Environment and Climate Change Canada, Toronto, ON, Canada
[2]NASA Goddard Space Flight Center, Greenbelt, MD 20771, USA.
[3]LuftBlick, Innsbruck, Austria.
[4]Department of Atmospheric and Cryospheric Sciences, University of Innsbruck, Innsbruck, Austria.

Correspondence to: Xiaoyi Zhao and Vitali Fioletov (xiaoyi.zhao@ec.gc.ca and vitali.fioletov@ec.gc.ca)

Abstract. Ground-based remote sensing instruments have been widely used for atmospheric research but applications for air quality monitoring remain limited. Compared to an in situ instrument that provides air quality conditions at the ground level, most remote sensing instruments (nadir viewing) are sensitive to a broad range of altitudes, often providing only integrated column observations. These column data can be more difficult to interpret and to relate to surface values and hence to "nose-height-level" health factors. This research utilized ground-based remote sensing and in situ air quality observations in ~~the Canadian~~ Canada's Athabasca Oil Sands Region to investigate some of their differences.

Vertical column densities (VCDs) of SO_2 and NO_2 retrieved by Pandora spectrometers located at the Oski-Otin site at Fort McKay~~,~~ (Alberta, Canada), from 2013–2019 were analyzed along with measurements of SO_2 and NO_2 surface concentrations and meteorological data. Aerosol optical depth (AOD) observations by CIMEL sunphotometer were compared with surface $PM_{2.5}$ data. The Oski-Otin site is surrounded by several large bitumen mining operations within the Athabasca Oil Sands Region ~~(AOSR)~~ with significant NO_2 emissions from the mining fleet. Two major bitumen upgraders that are 20 km south-east of the site have total SO_2 and NO_2 emissions of about 40 kt yr^{-1} and 20 kt yr^{-1} respectively. It was demonstrated that remote sensing data from Pandora and CIMEL combined with high vertical resolution wind profiles can provide information about pollution sources and plume characteristics. Elevated SO_2 VCDs ~~are~~ were clearly observed for times with south and south-eastern winds, particularly at 200–300 m altitude (above ground level). High NO_2 VCD values were observed from other directions (e.g., north-west) with less prominent impacts from 200–300 m winds. In situ ground observations of SO_2 and NO_2 show a different sensitivity with wind profiles, indicating they are less sensitive to elevated plumes than remote sensing instruments. In addition to measured wind data and lidar observed boundary layer height (BLH), modelled wind profiles and BLH from ECMWF Reanalysis v5 (ERA-5) have been used to further examine the correlation between column and surface observations. The results show that the height of emission sources (e.g., emissions from high stacks or near surface)

will determine the ratio of measured column and surface concentration values (i.e., could show positive or negative correlation with BLH)., which depends on the height of emission sources (e.g., emissions from high stacks or near surface). This effect will show impacts on the comparison between column observations (e.g., from the satellite or ground-based remote sensing instruments) with surface in situ measurements.

5   This study explores differences between remote sensing and in situ instruments in terms of their vertical, horizontal, and temporal sampling differences. Understanding and resolving these differences are critical for future analyses linking satellite, ground-based remote sensing, and in situ observations in air quality monitoring and research.

1. Introduction

Satellite measurements have been widely used to analyze long-term changes and trends in atmospheric air pollutants such as
10   sulphur dioxide (SO_2) and nitrogen dioxide (NO_2) (Barkley et al., 2017; Duncan et al., 2016; Krotkov et al., 2016; Liu et al., 2017; McLinden et al., 2016; Song and Yang, 2014; Wang et al., 2015) and to estimate the corresponding emission rates (Fioletov et al., 2011, 2015; de Foy et al., 2015; Lu et al., 2015; Streets et al., 2013). It is expected that satellite instruments will play an even bigger role in air quality monitoring in the future (new high-resolution geostationary missions such as TEMPO (Zoogman et al., 2017), Sentinel 4 (Gulde et al., 2017) and GEMS (Kim et al., 2020)). However, there is a major
15   complication in applying satellite measurements to surface air quality applications. Most nadir viewing satellite instruments are sensitive to the entire atmospheric column and hence derive vertical column densities (VCD; vertically integrated number density of a given species from the bottom to top of the atmosphere) and their conversion to surface concentrations required by air quality applications is not straightforward.

Ground-based remote sensing observations of the same quantity help both to validate satellite observations and
20   facilitate a better interpretation of satellite data and their links to surface concentration (Richter et al., 2013), keeping in mind the mismatch between satellite and ground-based remote sensing quantities that was widely reported (Herman et al., 2009; Judd et al., 2020; Kollonige et al., 2017; Zhao et al., 2020, 2022). Alternatively, a direct comparison of ground-based VCD observations with surface concentrations does not typically produce high correlations even in polluted urban areas (Dieudonné et al., 2013). Taking the planetary boundary layer (PBL) height into account improves the agreement between in situ and VCD-
25   derived surface mixing ratios for NO_2, but not so much for SO_2 (Knepp et al., 2015). Other efforts to convert ground-based VCD measurements to surface concentrations were made by researchers via various approaches, including applying convertion conversion ratio factors (e.g., Kollonige et al., 2017; Zhao et al., 2019). However, due to some fundamental differences between ground-based remote sensing and in situ instruments (e.g., sampling difference in space and frequency), surface concentration estimates via these instruments still have non-negligible biases difference (e.g., surface NO_2 derived from Pandora observations
30   has about -7% bias compared to in situ data; Zhao et al., 2019). One of the major challenges is the difficulty in modelling,

2

measuring, or estimating the boundary layer conditions (e.g., boundary layer height (BLH), wind speed and direction profiles) that is critical to resolving the vertical structure of air pollutants (e.g., Zhao et al., 2019).

The mining and refinery operations in the Athabasca Oil Sand Region ~~(AOSR)~~ are one of the largest sources of atmospheric pollutants in Canada. Environmental and health concerns associated with oil sands operations, including air

5 quality and acid deposition, are well known (e.g., Kelly et al., 2010). SO_2 and NO_2 are on the top of the list of gaseous pollutants emitted from the oil sands and highly elevated levels of these pollutants over the oil sands area have been detected (Simpson et al., 2010). Due to the large size of the oil sands operation area, satellite column measurements are an attractive method for air pollution monitoring in this region and satellites have been used for monitoring SO_2 and NO_2 emissions and trends in ~~AOSR~~ this region (McLinden et al., 2012, 2014, 2016, 2020). The oil sands operation activities north and south of the Oski-Otin site

10 at Fort McKay ~~in AOSR~~ make the pollution conditions highly dependent on wind direction on certain altitudes.

To better establish the link between column and surface concentrations observations, we examined seven years of ground-based remote sensing column observations along with surface concentration measurements, vertical wind profile and BLH observations, and reanalysis model data at the Oski-Otin site. In this work, vertical column of SO_2 and NO_2 are provided by Pandora spectrometer (Fioletov et al., 2016; Herman et al., 2009); aerosol optical depth (AOD) are provided by CIMEL

15 sunphotometer (Holben et al., 2001; Sioris et al., 2017); SO_2, NO_2, and $PM_{2.5}$ surface concentration values are from Thermo 43i, 42i, and Teledyne API T640, respectively. Collocated wind profiler and lidar instrumentation (Strawbridge et al., 2018) allow for examining the VCD dependence on the wind speed and direction at different altitudes and linking the VCDs to surface concentrations ratio with observed BLH. Besides trace gas pollutants, we also compared and ~~study~~ studied the differences between surface $PM_{2.5}$ observations with remote sensing AOD data. $PM_{2.5}$ concentration is also one of the three

20 indicators in the Canadian Air Quality Health Index (Stieb et al., 2008). Remote sensing observations of aerosols face more challenges than ozone and NO_2 (e.g., Herman et al., 2009; Jeong et al., 2020).

In short, this study is focused on the difference between total column (measured using ground-based remote sensing technique) and surface/ground-level concentrations (by in situ observations) of air pollutants. Measurements of wind profiles and BLH were used to examine their impact on that difference. The possibility of using modern reanalysis-modelled data

25 instead of direct measurements of wind profiles and BLH were also explored. ~~Utilizing information on detailed vertical wind field profiles and BLH, this work illustrates the cause and demonstrates the differences between ground-based remote sensing and in situ observations, as well as studies the ratios of the surface to column values for various wind directions and BLH values.~~

This paper is organized as follows: Sect. 2 describes the ground-based remote sensing observations and in situ

30 measurements. In Sect. 3, the observation conditions (mainly weather) induced differences are evaluated. In Sect. ~~3~~4, the vertical sampling difference between remote sensing and in situ measurements are evaluated by integrating the data with wind profiles ~~for SO_2, NO_2, and aerosols respectively~~. ~~Horizontal transports of pollutants are evaluated with wind speed and~~

directions in Sect. 4 to understand their transport patterns. Sect. 4 also focuses on how meteorological conditions can affect the sampling differences between remote sensing observations and in situ measurements. Sect. 5 shows the potential of using reanalysis meteorological data to help interpret the ground-based remote sensing observations. In Sect. 6, the integration period differences are evaluated. Conclusions are given in Sect. 76.

5 2. Observation sites and datasets

The Oski-Otin site at Fort McKay (57.184°N, 111.64°W) is equipped with various instruments for air quality measurements (e.g., Strawbridge, 2013; Fioletov et al., 2016; McLinden et al., 2020). Fort McKay is a small town (population of 600) surrounded by seven oil sands surface and two in-situ mining facilities to the north and south. Satellite maps for the observation site and surrounding oil sands areas are shown in Fig. 1. There are two major SO_2 and NO_2 sources located south of Fort

10 McKay: The Syncrude Mildred Lake plant is located 16 km to the south of Fort McKay and the Suncor Millenium Plant is 23 km south-south-east. According to the National Pollutant Release Inventory (NPRI, https://www.canada.ca/en/services/environment/pollution-waste-management/national-pollutant-release-inventory.html, last accessed on Sept. 10, 2023), the 2013–2019 annual mean emissions were about 26 kt (14 kt) and 17 kt (5.8 kt) of SO_2 (NO_2) per year from the Syncrude and Suncor facilities, respectively. McLinden et al. (2020) reported discrepancies in NPRI and the

15 satellite-derived SO_2 emissions in AOSRthis region, peaking at 50 kt yr^{-1} around 2016 (i.e., NPRI underestimated the emissions; Pandora instrument measurements showed agreement with satellite observations). There is also the Horizon Oil Sands processing plant and mine 18 km to the north, but the emissions from that source are smaller (4 kt of SO_2 and 1.4 kt of NO_2 per year). For NO_2, there are however many other small local sources. In addition, there are major NO_2 emissions from local sources as well as from the mining areas caused by the off-road heavy vehicle fleet that excavates and transports bitumen

20 from the mines to the on-site separation facilities. There are hundreds of kilometres of pristine boreal forests to the west and east from the Oski-Otin siteFort McKay with no SO_2 and NO_2 sources. Thus, the pollution level at the site Fort McKay is largely dependent on the wind direction. In situ data from Fort McKay can be found from the Wood Buffalo Environmental Association (WBEA) (site AMS 01; https://wbea.org/ last accessed on Sept. 10, 2023) Therefore, the planning of communities close to industrial activities should consider regional climatology factors, such as prevailing wind directions.
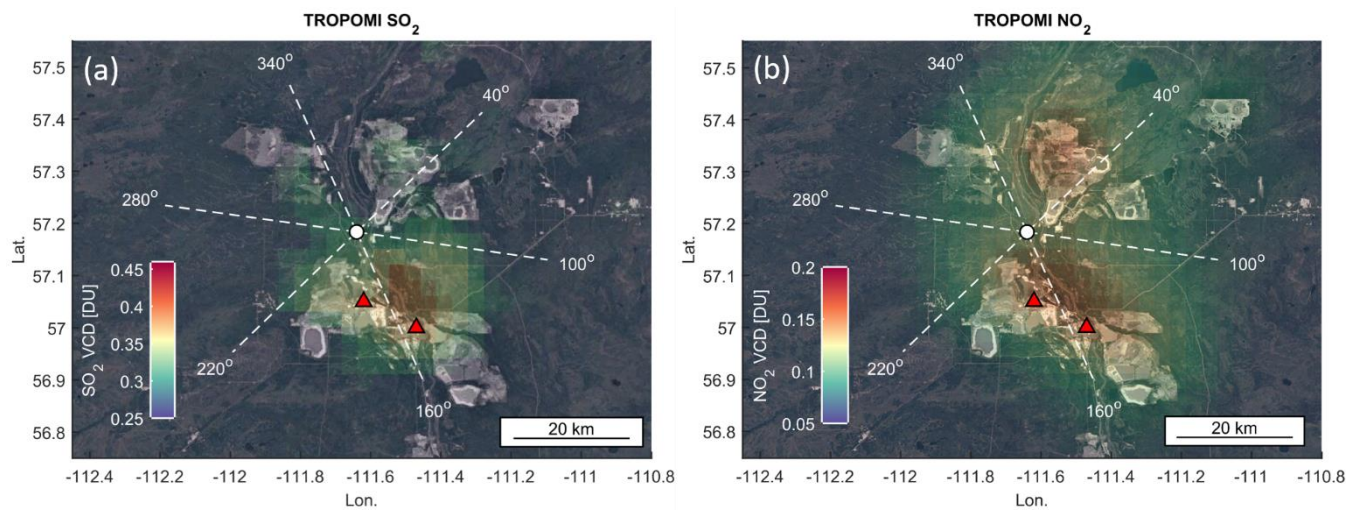
4

Figure 2~~1~~, Satellite maps (© Google Maps) of the Athabasca Oil Sand Region ~~(AOSR)~~ masked with satellite observations~~selected wind directions~~. The Pandora spectrometer, sunphotometer, WindRASS, lidar, and in situ instrument were located at the observation site represented by a white circle. The two largest upgraders in the mining areas are shown by red triangles. The white dashed lines show the centre of the wind sectors. Maps are masked with pixel averaging of total column SO_2 and tropospheric column NO_2 (2018–2021) from TROPOMI satellite instrument (McLinden et al., 2020).

2.1 Pandora

The Pandora spectrometer is ~~a recently developed~~a ground-based remote sensing instrument that measures solar and sky spectral radiation in the UV and visible part of the spectrum (Herman et al., 2009; Szykman et al., 2019). Direct sun (DS) measurements are the main type of observations, although ~~it~~ the instrument is also capable of operating in the zenith sky (ZS) and multi-axis differential optical absorption spectroscopy (MAX-DOAS) modes (e.g., Zhao et al., 2019; Kreher et al., 2020). In this work, vertical column densities of trace gases are derived from the DS measured spectra. It has been demonstrated that Pandora can successfully observe total column ozone ~~and~~, NO_2 (Herman et al., 2009, 2015; Tzortziou et al., 2012, 2015; Zhao et al., 2016, 2020), and SO_2. ~~In 2013, a Pandora instrument, along with other instrumentation, was deployed to the AOSR and its measurements were used to establish optimal retrieval procedures for the SO_2 VCD measurements and estimate measurement uncertainties~~ (Fioletov et al., 2016). The integrated vertical column values of trace gases are reported in Dobson Units (DU; $DU = 2.69 \times 10^{16}$ molecules cm^{-2}).

~~The Pandora instrument consists of an optical head sensor, mounted on a computer controlled sun tracker, and connected to a commercial Avantes array spectrometer by means of an optical fibre. To allow for the detection of different absorbers, the instrument periodically measures UV spectra with the U340 bandpass filter with a cut-off limit at 380 nm on and off, with an interval of about 90 seconds. The 306–330 nm spectral interval was used for SO_2 spectral retrievals (ECCC~~

5

~~research retrieval) and the 400 to 440 nm interval was used to retrieve NO₂ (PGN official retrieval, version nvs1p1-7) (Fioletov et al., 2016; Zhao et al., 2020). The integrated vertical column values of trace gases are reported in Dobson Units (DU; DU = 2.69×10¹⁶ molecules cm⁻²). Pandora instrument no. 104 was deployed to Fort McKay in the oil sands region, where it was operating from August 15, 2013 to November 14, 2013. It was then redeployed on August 21, 2014, and was operational until late 2015 (Zhao et al., 2016). From September 2017 to 2020, Pandora no. 122 was deployed at the site. The Pandora no. 122 was operated with multi-axis observations (in addition to DS and ZS) since 2018, but no SO₂ or NO₂ profile has been retrieved from these observations yet. The operation of Pandora at the site stopped in summer 2020.~~

A detailed description of the Pandora spectrometer and its total column NO_2 retrieval algorithm is given by ~~(~~Herman et al.~~,~~ (2009). ~~In order to~~To isolate tropospheric NO_2 VCD from the total column VCD measured by Pandora, stratospheric NO_2 partial columns were subtracted from Pandora measurements (~~using OMI satellite data and the Pratmo box model~~following the method described in ~~;~~ Zhao et al., 2019). For the observation period in the oil sands region, typically, stratospheric NO_2 accounts for about 46% of the total column (median value), with a standard deviation of 35%. For convenience, we refer to this tropospheric NO_2 VCD as simple "NO_2 VCD". Information about the instrument set up at the Oski-Otin site ~~Fort McKay~~ and the SO_2 data and algorithms are available from Fioletov et al., (2016). For SO_2 data, as the only sources are near the surface (as no comparable SO_2 quantities were in the stratosphere during the analyzed period, i.e., no SO_2 injection from volcanic eruptions), the retrieved total column SO_2 (SO_2 VCD from Pandora observations) ~~are~~were directly ~~been~~ used in this study.

Pandora instrument no. 104 was deployed to the Oski-Otin site ~~Fort McKay in the oil sands region, where it was operating~~ from August 15, 2013 to November 14, 2013. It was then redeployed on August 21, 2014, and was operational until late 2015 (Zhao et al., 2016). From September 2017 to 2020, Pandora no. 122 was deployed at the site. The Pandora no. 122 was operated with multi-axis observations (in addition to DS and ZS) since 2018, but no SO_2 or NO_2 profile has been retrieved from these observations yet. The operation of Pandora at the site stopped in summer 2020.

2.2 CIMEL Sunphotometer

CIMEL ~~Sunphotometers~~ sunphotometers for measuring aerosol properties were deployed the Oski-Otin site since 2013, as a part of the AEROCAN network (Sioris et al., 2017). AEROCAN is the sub-network that consists of twenty sites across Canada within the Aerosol Robotic Network (AERONET, https://aeronet.gsfc.nasa.gov/ last access: 10 September 2023) that was established in the early 1990s (Holben et al., 2001). The sunphotometer measures AOD in direct sun mode at eight wavelengths, typically 340, 380, 440, 500, 675, 870, 940, and 1020 nm. AOD is a unitless quantity representing the vertically integrated extinction of radiation due to scattering and absorption of particles. To better quantify fine and coarse mode components of the measured AOD, spectral deconvolution algorithm (SDA) products were developed by O'Neil et al. (2003) based on the AOD spectral dependence and higher order spectral derivatives. Fine and coarse modes are essentially comprised

of sub-micron and super-micron particle radii, respectively (O'Neill et al., 2001). At the Oski-Otin siteIn Fort McKay, Sioris et al. (2017) reported that coarse mode aerosol and $PM_{2.5}$ only had low temporal correlation (as -0.02), while fine mode aerosol and $PM_{2.5}$ had much higher correlation (as 0.53). In this work, the fine mode aerosol (SDA Level 2 version 4.1; quality assured) outputs are used, which are processed from an operational product of AERONET.

2.3 WindRASS

The Radio-acoustic Sounding System (RASS) wind profiler (WindRASS; model MFAS, Scintec, Rottenburg, Germany) was another instrument installed at the Oski-Otin site (Gordon et al., 2018; Strawbridge et al., 2018). It reports wind speed and direction as well as other meteorological parameters as 15-minute averages, at 77 levels from 40 m to up to 800 m above ground (10 m vertical resolution). It is a monostatic 64-transducer sodar that emits sound pulses near 2000 Hz vertically and in the four cardinal directions (tilted at 22° and 29° from zenith). The radio antennas then emit electromagnetic waves (915 MHz) that are partially reflected by the sound waves as they propagate away into the atmosphere. Doppler analysis of the returning signal is used to reconstruct the temperature profile (based on the fact that the speed of sound is a function of the square root of the virtual temperature) as well as the 3-D wind vector. Note that the number of successful WindRASS observations depends on the altitude and the vertical range varies from measurement to measurement as discussed in Appendix A.

2.4 Lidar

An autonomous lidar system that can be monitored remotely and operated continuously (except during precipitation events) was also installed at the Oski-Otin site since 2013 (Strawbridge, 2013). The lidar simultaneously emits two wavelengths laser light (1064 and 532 nm, Q-switch *Neodymium-doped Yttrium Aluminum Garnet*Nd:YAG, see references in Strawbridge, 2013) at energies of approximately 150 mJ pulse^{-1} wavelength^{-1} and detects the backscatter signal at 1064 nm and 532 nm (and both polarizations at 532 nm). Since 2016, the lidar system was upgraded by adding an ozone DIAL (Differential Absorption Lidar) to simultaneously measure the vertical profile of tropospheric ozone, aerosol (at 355, 532, and 1064 nm) and water vapour (through the addition of the 355 nm output channel to the aerosol lidar) from near the ground to 10 to 15 km (Strawbridge et al., 2018). The BLH was derived via the 532 nm aerosol lidar profile. Details on the BLH processing algorithm can be found from Strawbridge and Snyder (2004).

2.5 In situ measurements

In this study, we used the in situ measurements of SO_2, NO_2, $PM_{2.5}$, NOx, and O_3 as well as the wind speed and direction data provided by the Wood Buffalo Environmental Association (WBEA; https://wbea.org/, last accessed on Sept. 10, 2023). The list of analytical equipment that have been used can be found at https://wbea.org/wp-content/uploads/2021/03/Bertha-Ganter-

Fort-McKay-Site-Documentation_2021.pdf (last accessed on Sept. 10, 2023). Surface SO_2 and NO_2 were measured by Thermo Scientific 43i and 42i instruments with a precision of 1 and 0.4 ppbv, respectively. $PM_{2.5}$ were measured by Teledyne API T640 instrument with a precision of 0.5 µg m^{-3}. The Level 2 data (hourly) that has undergone validation review are used in this work. Pandora spectrometer, CIMEL sunphotometer, and WindRASS data were averaged into hourly resolution to match

5   with sampling rate of in situ Level 2 data. The statistics of measured pollutants are summarized in Table 1.

Table 1. Statistics of measured pollutants.

Pollutants	Measurement sources for comparisons	Mean (median)	Standard deviation	Uncertainties
Sulphur Dioxide (SO_2)	Pandora (column in DU)	0.22 (0.10)	0.54	0.05
	In situ (surface concentration in ppbv)	1.09 (0.35)	3.15	1
Nitrogen Dioxide (NO_2)	Pandora (column in DU)	0.16 (0.14)	0.15	0.001
	In situ (surface concentration in ppbv)	7.40 (4.42)	7.98	0.4
Aerosol	Sunphotometer AOD (column, unitless)	0.10 (0.06)	0.19	0.02
	In situ $PM_{2.5}$ (surface concentration in µg m^{-3})	8.59 (5.16)	37.75	0.5

2.6 ERA-5 Reanalysis meteorological data

10   In this work, ECMWF Reanalysis v5 (ERA-5) wind data (hourly, using model-levels as the vertical co-ordinate) are utilized in addition to WindRASS observations. Several studies have verified that ERA-5 wind data can facilitate remote-sensing-based emission estimations (e.g., Fioletov et al., 2015; McLinden et al., 2020), regional air quality monitoring (e.g., Liu et al., 2021; Tzortziou et al., 2022; Zhao et al., 2022), and wind-based satellite validation (Park et al., 2022; Zhao et al., 2020). To assess whether ERA-5 wind can be a good replacement for near-surface to free troposphere vertical wind measurements, the

15   ERA-5 model level data (Hersbach et al., 2020) were used (instead of its pressure level data, which is more commonly used). It is worth noting that for ERA-5 pressure level wind data, there are only ~~5~~ five wind layers from 900 to 1000 hPa (900, 925, 950, 975, and 1000 hPa). While using ERA-5 model level data, there are about 11 to 18 modelled wind layers from 900 to 1000 hPa, for the Oski-Otin site. Thus, ERA-5 model level data can provide a much more detailed vertical wind field than pressure level data. In addition to wind data, the boundary layer height from ERA-5 has also been used to examine the

20   correlation between column and surface observations.

3. Integration period differences

Figure 2 shows the time series of observed column and surface concentrations of SO_2, NO_2, and aerosol at the Oski-Otin site. Compared to surface concentration observations that practically have no gaps, column data records have gaps due to instrumental issues and other operational changes as well as due to the clouds. Thus, only coincident (overlapped) observations from both the surface and column data were included in the analysis.
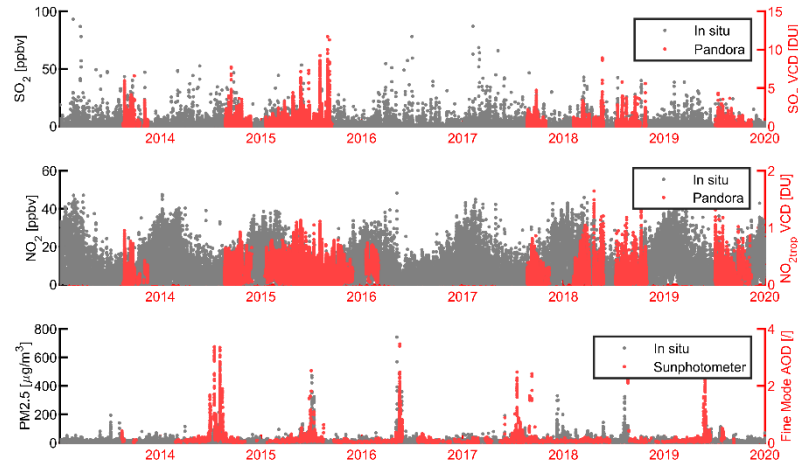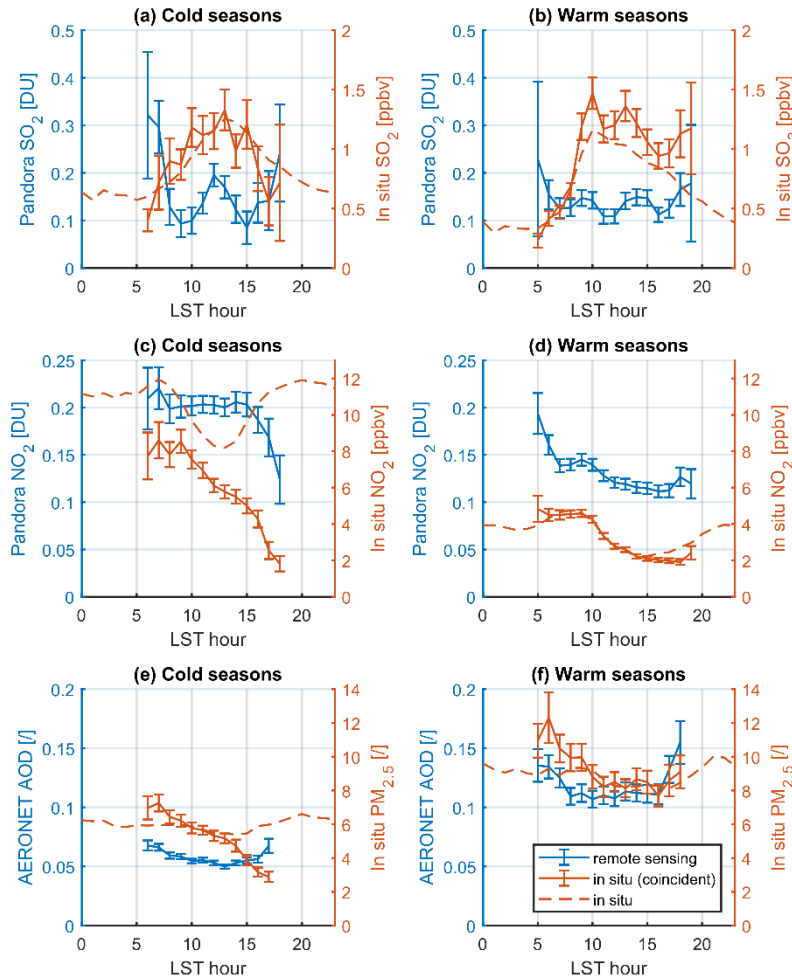

Figure 2. Time series of remote sensing and in situ observations of SO_2, NO_2, and aerosol data at the Oski-Otin site.

In contrast to in situ instruments that can obtain 24 hr continuous observations, passive remote sensing instruments (i.e., use the sun as a light source) ~~can only~~ deliver data when direct solar light can reach the instruments. Figure ~~12~~3 shows the coincident observations ~~from remote sensing (blue solid lines with error bars) and in situ (red solid lines with error bars) observations~~ that have been averaged by the hour (local standard time). Both SO_2 and NO_2 data show good agreement in variation patterns except early morning. The prominent discrepancy in the morning could be related to larger changes in the mixing layer height and related vertical mixing conditions. For example, in cold seasons, with increased mixing layer height and vertical dynamics from the morning to noon, in situ SO_2 shows a strong increase from 0.40 ppbv at 6 am to 1.18 ppbv at 10 am (see Fig. ~~12~~3). In contrast, the Pandora observations show an opposite decreasing trend; the VCD of SO_2 decreased from 0.32 DU at 6 am to 0.01 DU at 10 am. As discussed before, Pandora can sample the entire vertical column of SO_2 molecules, thus the increase of surface SO_2 concentration (from less than 0.5 ppbv at 6 LST to almost 1.5 ppbv at 10 SLT) in the morning (see Fig. ~~12~~3b, in the warm seasons) is not due to increased emission (SO_2 VCD values are stable from 6 to 10 LST) but due to vertical mixing. Better vertical mixing conditions in the late morning to noon help the elevated SO_2 plume to

9

reach the surface level. With a well-mixed boundary layer after 10 am, the variation pattern of surface and column values of SO$_2$ shared a similar pattern.

The conditions for NO$_2$ are similar to those for SO$_2$ but show stronger indications from photochemistry, i.e., generally decreased values of NO$_2$ from morning to evening. Moreover, as there are strong NO$_2$ sources near ground level, even the

VCD are stable from 8 to 15 LST (e.g., see ~~Figs. 12~~ Figs. 3b), while the surface value is ~~keep~~ decreasing. For aerosol comparison, both AOD and $PM_{2.5}$ show clear U-shape changes over the day in warm seasons (see Fig. ~~12~~3f). However, in the afternoons of cold seasons, $PM_{2.5}$ shows a decreasing trend, while AOD has an increasing trend (see Fig. ~~12~~3e). Thus, without detailed meteorological information (e.g., BLH and vertically resolved wind information), ~~there~~ it is of no surprise that we could not find an easy and clear correlation between remote sensing and in situ ~~observations~~ diurnal variations.

  In addition to data sampled at the time of measurements by remote sensing instruments, results based on all in situ measurements are plotted in Fig. ~~12~~3 as red dash lines. When comparing red dash lines with red solid lines, the results from Fig. ~~12~~3 ~~shows~~ show interesting and prominent features, i.e., when pairing in situ data with remote sensing data, sometimes, the diurnal patterns of in situ measurements are changed (e.g., see Fig. ~~12~~3c, the different variations of the red solid and red dashed lines). The cause of such changes is due to the "sampling bias" from remote sensing measurements that are available under unobscured sun conditions only; in situ data has no major gaps. Although the local emissions conditions might not be different in sunny or rainy days, the difference in meteorological conditions can affect the pollutants monitoring results. For example, Fig. ~~13~~4 shows the ERA-5 boundary layer height data binned by hours of local standard time. The BLH data that are coincident with in situ SO_2 measurements show clear seasonal difference (see blue lines in Figs. ~~13~~4a and b); in cold seasons, the highest BLH data only reach 750 m, while in warm seasons it can reach 1500 m. The diurnal variations of BLH data show bell curves as in situ instruments performs sampling 24 hr per day in all weather conditions. However, the BLH data that are coincident with remote sensing SO_2 measurements (see red lines in Figs. ~~13~~4a and b) show more skewed shapes, i.e., higher BLH values in afternoons. Especially, in the wintertime (Fig. ~~13~~4a), BLH data that coincident with remote sensing observations ~~shows~~ show a much stronger increasing from 10 to 16 LTS (local standard time) than its counterpart that is coincident with in situ measurements. Similar features can be seen for NO_2 and aerosol data. Thus, ~~it is clear that~~ remote sensing observations are biased to high BLH conditions, especially in afternoons. These results also explain why, when coincident with remote sensing observations, in situ diurnal patterns changed (see Fig. ~~12~~3). For example, in cold seasons at 17 LST, by pairing $PM_{2.5}$ data with AOD data, the corresponding BLH value increased from 500 m to 1500 m (see Figs. ~~13~~4e) and thus the $PM_{2.5}$ values changed from 6.0 µg m^{-3} to 2.9 µg m^{-3} (see Fig. ~~12~~3e). Such variation in diurnal patterns is not obvious in warm seasons, due to less BLH changes (due to coincident selection with remote sensing instrument) than cold seasons. For instance, by selecting coincident measurements, measured NO_2 surface values dropped from 11.3 pptv to 2.5 pptv in cold seasons at 17 LST (Fig. ~~12~~3c); while the corresponding values only dropped from 2.5 pptv to 2.0 pptv, in warm seasons (Fig. ~~12~~3d). In other words, the sampling biases between remote sensing and in situ data are worse in cold seasons than warm seasons. When direct comparing coincident remote sensing and in situ observations, such weather condition biased sampling would not easily been revealed. However, this clear-sky bias could lead to significant differences in long-term trend analysis.

  In short, ~~similar to findings in Sects. 3 to 5,~~ Figs. ~~12~~3 and ~~13~~4 show that depending on the height of the emission sources, boundary layer dynamics can play important roles in the sampling differences between remote sensing and in situ

11

instruments. Modelling of boundary layer conditions is also known to be a major difficulty for air quality modelling work (e.g., Zhao et al., 2019). This indicates a great need for improved boundary layer height observations from other remote sensing instruments (Szykman et al., 2019). This issue could be more prominent if the remote sensing air quality measurements are performed in the urban area, where rush hour air pollutants are often more serious on cold winter. All these bring great challenges to utilizing remote sensing air quality observations for application to "noise-height" air quality monitoring and more efforts are needed.

5
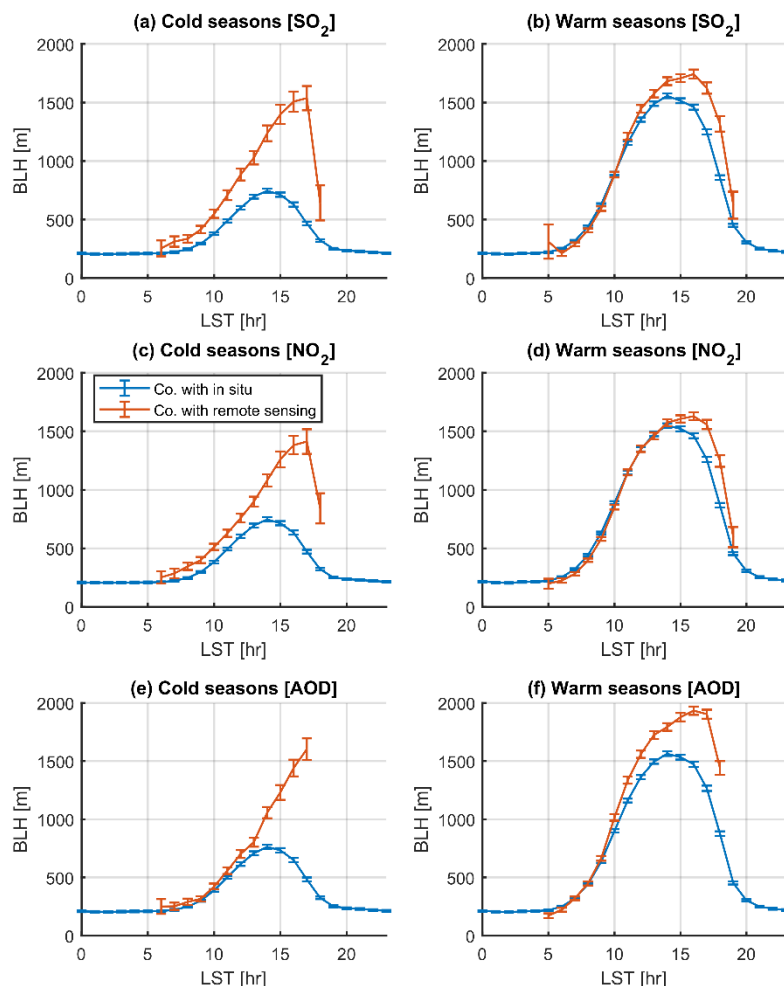
Figure 134. Boundary layer height (BLH) data averaged by the hour of local standard time (LST). Blue lines show BLH mean values that based on all data; red lines show BLH data that are coincident with remote sensing observations, i.e., when the

12

~~3~~4. Vertical sampling differences between remote sensing and in situ observations

~~Figure 1 shows the time series of remote sensing and in situ observed SO₂, NO₂, and aerosol data in Fort McKay. Compared~~
5   ~~to in situ observations that practically have no gaps, remote sensing data records have gaps due to instrumental issues and other~~
~~operational changes as well as due to the clouds. Thus, only coincident observations from both remote sensing and in situ~~
~~instruments were included in the analysis.~~
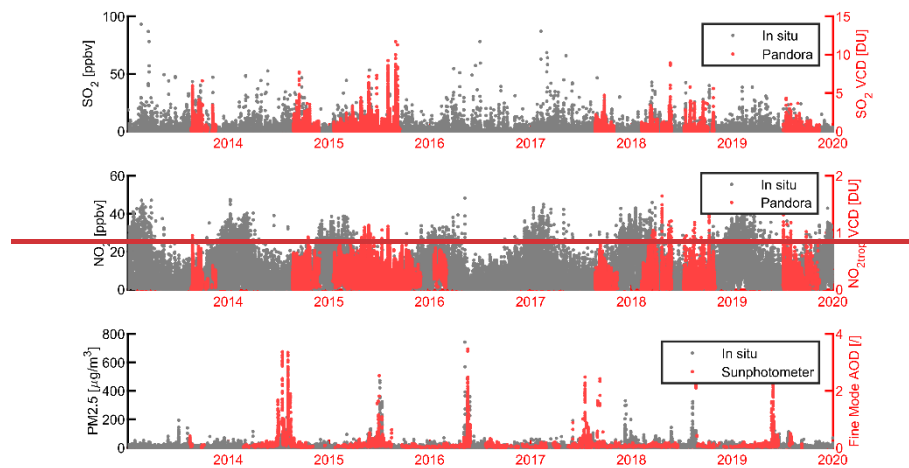
Figure 1. Time series of remote sensing and in situ observations of SO₂, NO₂, and aerosol data at Fort McKay.

10   ## ~~3~~4.1 Sensitivity of SO₂ observations to winds at different levels

For the Pandora located at Oski-Otin site, higher SO_2 VCDs for southern wind direction were previously reported based on the surface winds (Fioletov et al., 2016). Utilizing SO_2 VCD observations, various satellite measured SO_2 plume reconstructions work (e.g., McLinden et al., 2020) has been done to estimate the emissions (e.g., Fioletov et al., 2015, 2020). Typically, in those plume models, the vertical structure of the SO_2 plume is not considered, as satellites measure the integrated
15   column of the SO_2. However, to link the surface and satellite observations, information of the vertical structure of the SO_2 plume or other pollutants are critical. If the plume is elevated, it is not necessarily true that the direction of surface winds would be correlated with the VCDs; the wind direction at the plume height would be a more important factor. For the surface in situ instruments, this effect would not be prominent (i.e., in situ instruments are expected to most sensitive to near surface wind). To test that, we calculated mean VCDs for data binned by the wind altitude and direction using the wind profiler data. If the
20   mean SO_2 VCD values are the same for all wind directions, then winds at that height do not affect SO_2 transport. And the

13

larger the spread of the mean SO$_2$ VCD values for different directions, the greater impact from winds at that height is for SO$_2$ transport. This information can be used to determine what wind directions and at what altitudes have the largest impact on VCDs and thus for pollutant transports.

5

10   ~~A map of the AOSR is shown in Fig. 2, with selected wind directions plotted.~~ The wind direction bins were selected to have one bin centred at 160° where the SO$_2$ signals have a maximum from the two major upgraders (Fig. 1, see red triangles on the map). Elevated SO$_2$ plumes from these upgrader stacks were also observed and reported by a MAX-DOAS instrument in previous studies (e.g., Davis et al., 2020). The heights of these stacks are in the range of 76–183 m (Gordon et al., 2018). Davis et al. (2020) reported the retrieved SO$_2$ plume can reach 30 ppbv concentration at 395 m height.

15   Figure ~~3a~~ 5a shows the mean SO$_2$ VCD for data binned into 60°-wide wind direction bins based on WindRASS wind data from each 10 m altitude level. In other words, Fig. ~~3a~~ 5a shows the results of binning measured SO$_2$ VCDs with wind information from different vertical wind layers; Fig. ~~3a~~ 5a is not depicting actual vertical profiles of SO$_2$, but an illustration of which layer of measured wind profile has the highest impact on SO$_2$ column and surface observations. The values are the highest for winds out of the south-south-easterly (SSE; 160°) at all altitudes. The mean values are close to zero for the 40°,

20   280°, and 340° sectors. This dependence of VCDs on the direction is very similar to that of surface winds (Fioletov et al., 2016). The magnitude of the mean SO$_2$ VCD in both cold (Nov. to Apr.) and warm (May to Oct.) seasons reaches its maximum of 0.39 DU at 200–300 m; about 38% higher than the mean value for the same direction of surface or 40 m winds (0.25 DU). Thus, in the analyzed altitude range, the wind direction at 200–300 m has the largest impact on Pandora measured SO$_2$ VCD.

14

In contrast, for the clean air directions (280°) SO_2 VCD are the lowest regardless of the wind altitude. Also, wind data above 300 m (250 m for the cold season) were too intermittent to separate SO_2 VCD signals which indicate the SO_2 plumes were within this height (WindRASS vertical data recovery rate is shown in Fig. A1).

Compared to Pandora measured SO_2 VCDs, in situ SO_2 surface concentrations show a similar but not identical picture (see Fig. 3b5b). The in situ SO_2 observations show a similar increased sensitivity for winds at levels of 200–300 m with the same polluted and clean air directions as 160° and 280° respectively. However, the magnitude of the binned mean in situ SO_2 reaches its maximum of 3.16 ppbv for wind levels at 200–300 m is only about 27% higher than the mean value for the same direction at the surface layer winds (2.32 ppbv). The results indicate the different characteristics between the two measurement techniques of SO_2, i.e., VCD values are more sensitive to elevated plumes than surface values (i.e., the SO_2 emitted from high stacks of refineries in this case; 38% increased VCDs, while only 27% increased for surface concentrations, when using 200–300 m wind). In other words, in conditions that wind at 200–300 m are from 160°, on average, the observation yields the highest SO_2 VCDs, even if the plume is not fully vertically mixed to reach the ground level (see more discussion in Sect. 5.2).

As mentioned, the WindRASS wind profiler data have different number of successful observations at different heights. The number of available successful measurements as a function of altitude declines almost linearly. Only about 75% of all wind profiles reach 200 m and only 12% reach 400 m (see Fig. A1). Thus, the vertical structure revealed in Fig. 3 5 shows increased uncertainties for high altitudes (e.g., see increased width of the 1-sigma envelopes for profiles). This leads to a bias of wind profile observations that reach 500 m of altitude towards low wind speed conditions. Thus, tThe wind profile data from WindRASS is used only if it has full coverage within 0–300 m for both the warm and cold seasons, thus minimizing the wind speed bias while retaining the most sensitivity to to resolve air pollutant transport patterns in this region.
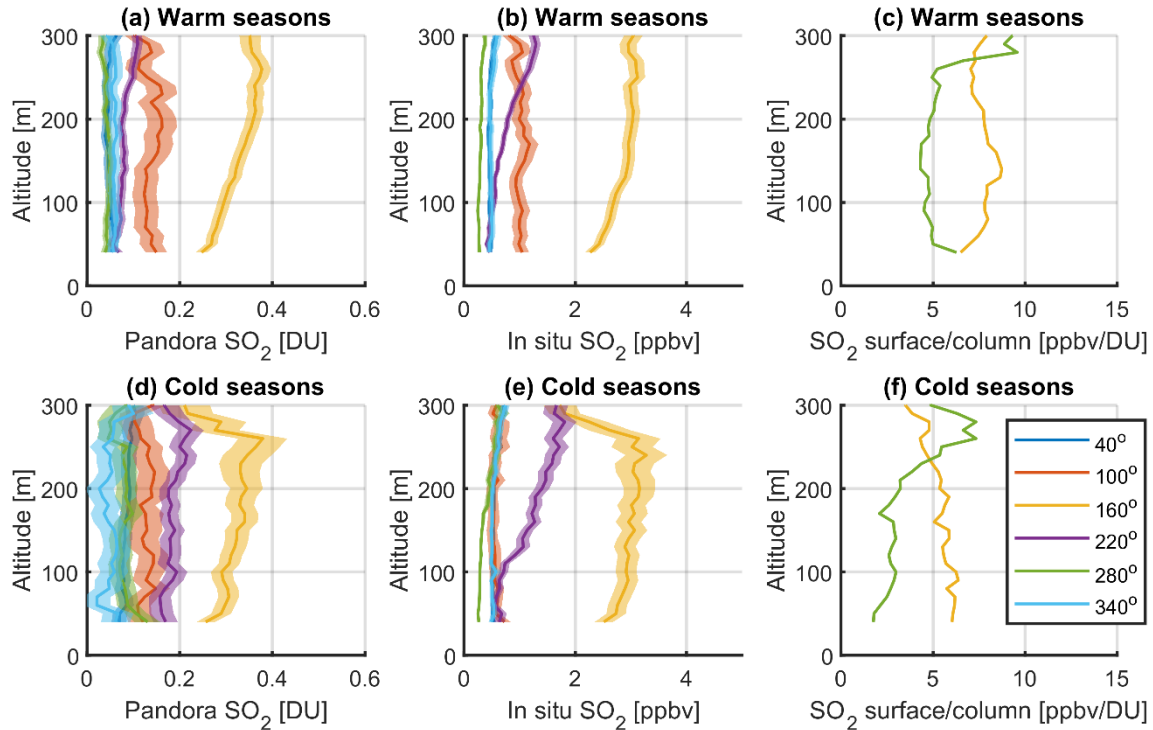
Figure 3_5_. The mean SO₂ column (a and d), surface (b and e) observations, and their median ratios (c and f) binned by wind directions at different altitudes at Oski-Otin. Wind layer information (altitude and direction) was measured by WindRASS, SO₂ column observations were from Pandora, surface measurements were from in situ instrument. Color lines show the mean values of SO₂ with 1-sigma envelopes. A sharp maximum can be found when the wind is from 160°, the directions to the upgraders. The wind direction bins were selected to have one bin centred at 160° where the SO₂ signals have a maximum. Data were categorized by warm (May to Oct.; top row) and cold (Nov. to Apr.; bottom row) seasons.

It is expected that the SO₂ plume height will be affected by boundary layer dynamics that are reflected by temperature and other seasonal meteorological aspects. Thus, the sensitivity of SO₂ VCD to the wind direction were categorized into warm (Figs. 3a 5a and b) and cold seasons (Figs. 3d 5d and e). Compared to the graduate decreasing sensitivity above "plume height" in warm seasons (i.e., 200–300 m), both remote sensing and in situ observations show their sensitivity to SO₂ emissions decreased sharply after passing the plume height in cold seasons (Figs. 5d and e). The results may indicate that the vertical transport of SO₂ is more refined within the boundary layer due to a lack of vertical mixing in cold temperatures. Note that, for warm and cold seasons, the median values of BLH from ERA-5 are 390 m and 208 m, respectively. Another interesting factor is the SO₂ plume from 220° is more prominent for in situ data (see the purple line in Fig. 2e 5e). However, there are no known strong SO₂ emission sources from this direction, and this feature is not captured by Pandora.

Figs.Figures 2c 5c and f show the ratio of observed surface concentration to column values (from 160° and 280°) grouped by the wind direction at different altitudes. For SO_2, this surface to column ratio preserved the pattern discussed above. Compared to the clean air directions (280°), such ratio values of the directions of the upgraders (160°) are much higher, indicating the SO_2 pollutants from the upgraders are less vertically mixed than its background conditions. However, more detailed features can be revealed if the data is further analyzed with BLH information (more details will be discussed in Sect. 5.2).

34.2 Sensitivity of NO₂ observations to winds at different levels

Analysis of NO_2 data is shown in Fig. 46. Similar to SO_2 VCD, the mean NO_2 VCD (tropospheric column, see description in Sect. 2.1) values are also the lowest for the westerly winds (280°) and the highest for the south-south-easterly winds (160°). The absolute maximum in the mean NO_2 VCD values is also observed for the 160° wind direction at 200–300 m, although this maximum is not as well-pronounced as in the case of SO_2. This may suggest that the NO_2 and SO_2 are coming from the same source, although there are other NO_2 sources in the area. Also, unlike SO_2, NO_2 VCD is also high from the 40° wind direction, i.e., from the north-eastern mining area (see Fig. 2b5b). Compared to the Pandora NO_2 observations, the in situ NO_2 data show more different results for its vertical sensitivity. Although the maximum NO_2 amount is still from 160°, in situ data is more sensitive to the wind layer heights in 50–100 m (Fig 4b6b, 160° result). A clear decreased sensitivity can be seen above 100 m with minimum values around 200–300 m. The results indicate Pandora is more sensitive to transported NO_2 than in situ instruments, while in situ instrument is more directly linked to preferred wind conditions (i.e., the near-surface wind must be from 160°). For the nearby source, i.e., 40°, both Pandora and in situ observations show similar straight vertical structures (see blue lines in Fig. 46). For the background observations (i.e., 280° and 340°, low NO_2 conditions), both Pandora and in situ observations show similar sensitivity for surface layer winds.
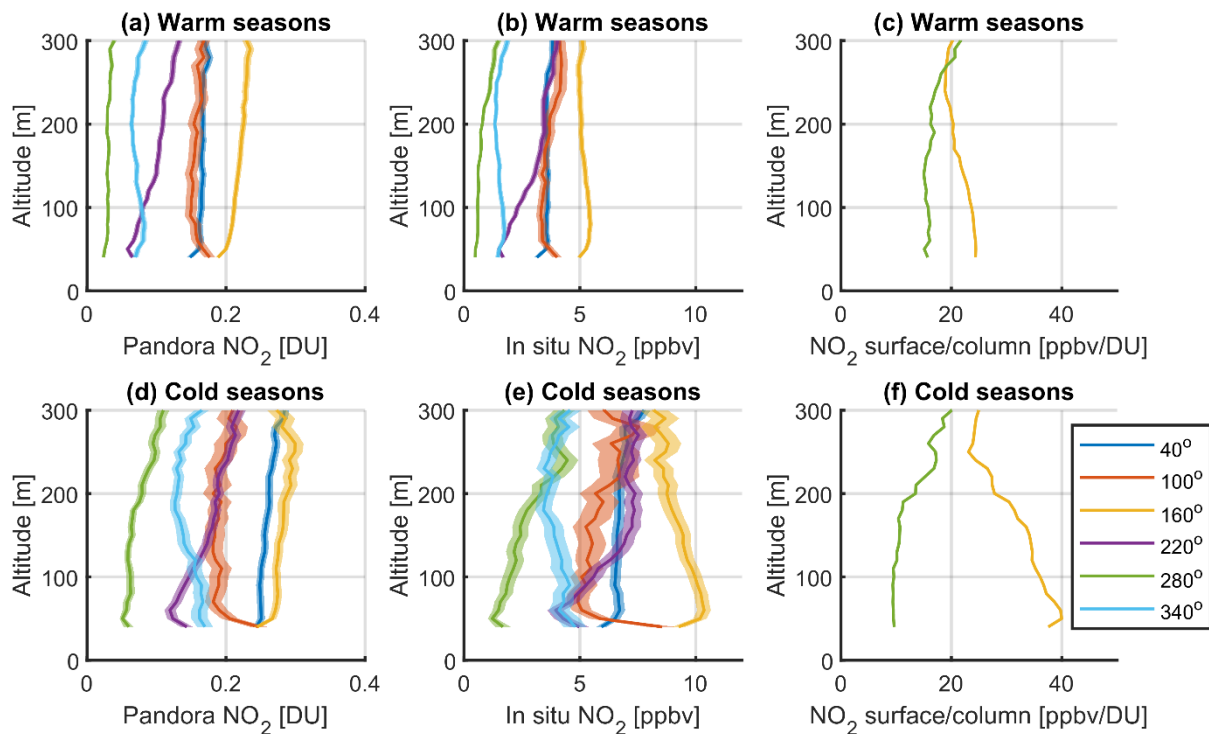
Figure 46. The mean NO₂ column (a and d), surface (b and e) observations, and their median ratios (c and f) binned by wind directions at different altitudes at Oski-Otin. Wind layers information (altitude and direction) were measured by WindRASS, NO₂ column observations were from Pandora, surface measurements were from in situ instrument. Color lines show the mean values of NO₂ with 1-sigma envelopes. Data were categorized by warm (May to Oct.; top row) and cold (Nov. to Apr.; bottom row) seasons.

An interesting feature that both in situ SO_2 and NO_2 analyses demonstrated is an enhanced sensitivity above 150 m in 220° wind directions (Figs. 2b 5b and 4b6b, purple lines). As the 220° wind bin covers the tailing ponds area and a large portion of the mining area (observations within 190°–250° wind directions), it is likely the observed transported emissions were from these areas. Thus, such 60° wind bins might be too coarse to separate some sources (fine bins were used to reveal horizontal transport in Sect. 4Appendix B, and no prominent emission sources were identified in 220° wind directions).

In general, by utilizing various ground-based remote sensing and in situ observations, such vertical sensitivity analysis can reveal the characteristic of air pollutants sources more efficiently than using in situ instrument only. When comparing the analysis results categorized by warm and cold seasons, the structures of vertical sensitivities show the changes due to different vertical dynamics. For example, in situ surface concentration data show more enhanced sensitivity for near-surface wind in cold seasons than in warm seasons (Figs. 4b 6b and 4e6e). However, even in cold seasons, Pandora data still preserved its sensitivity to transported emissions (200–300 m winds, compare yellow lines in Fig. 4d 6d and 4e6e), as it measures the integrated vertical columns. When comparing Figs. 4c 6c and 4f6f, the surface to column ratio at 70 m changes from 39

18

ppbv/DU in cold seasons to 24 ppbv/DU in warm seasons. The difference between polluted and clean air is also much larger in cold seasons, indicating a stronger inhomogeneity of tropospheric NO_2.

~~3~~4.3 Sensitivity of aerosol observations to winds at different levels

The sensitivity analysis of aerosol data to the wind ~~speed and direction~~profiles is shown in Fig. ~~5~~7. In contrast to SO_2 and NO_2
5   data, observations of aerosol data show greater differences between AOD and in situ $PM_{2.5}$ measurements, when they are binned by the wind direction. Similar to the Pandora instruments, the sunphotometer samples the aerosol through a slant light path (i.e., direct-sun viewing geometry, sample the atmosphere constituents between the instrument and the sun) and reports the vertically integrated column property. However, establishing the link between the AOD and $PM_{2.5}$ is more difficult (Sioris et al., 2017), compared to the work for trace gases observations since the AOD additionally depends on aerosol composition,
10   details of the size distribution, and even aerosol shape.

Similar to the SO_2 and NO_2 data analysis, the in situ $PM_{2.5}$ data show maximum sensitivity to the winds from 160°, indicating that most fine particles were from the direction of upgraders. However, the spread between the aerosol values from different directions is noticeably less than that for SO_2 and NO_2. But the vertical structure of $PM_{2.5}$ dependence on the 160° winds as a function of the wind height (Fig. ~~5b~~7b, orange line) is nearly the same from the surface to 300 m layers. Thus, the
15   $PM_{2.5}$ concentration under 160° wind direction was not sensitive to a particular layer of the wind. Comparing to the profiles of in situ SO_2 (elevated at 200–300 m; emissions from high stacks) and in situ NO_2 (two peaks, one near-surface and one elevated at 200–300 m; emissions from both near-surface mining fleet and high stacks) (see Figs. 5 and 6), the sources of $PM_{2.5}$ from this direction could not easily be distinguished. Comparing Figs. ~~5a~~7a and b, AOD data show higher sensitivity to winds from 100°, while $PM_{2.5}$ data show higher sensitivity to winds from 160°. These inconsistent results might be because the wind bins
20   were selected based on our knowledge of SO_2 and NO_2 sources, i.e., 100° and/or 160° wind bins might be mixed with several different sources of aerosols in this region. The AOD and in situ observations are in better agreement for other wind directions, i.e. they both show clean air (low aerosol) was from 280°.
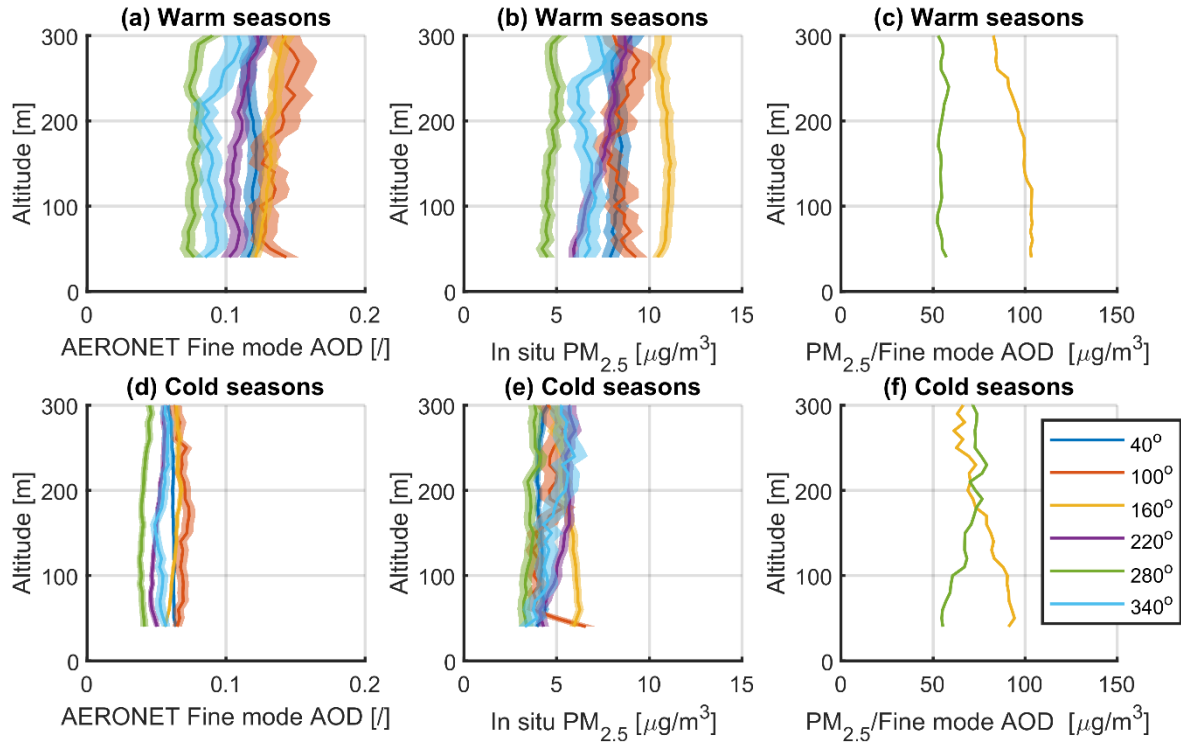
19

Figure 57. The mean aerosol column (a and d), surface (b and e) observations, and their median ratios (c and f) binned by wind directions at different altitudes at Oski-Otin. Wind layers information (altitude and direction) were measured by WindRASS, aerosol column observations (AOD) were from sunphotometer, surface measurements (PM$_{2.5}$) were from in situ instrument. Color lines show the mean values of aerosol with 1-sigma envelopes. Data were categorized by warm (May to Oct.; top row) and cold (Nov. to Apr.; bottom row) seasons.

In contrast to NO$_2$ results, which have increased surface concentration values in cold seasons, aerosol results reflect opposite patterns. AODs are smaller in cold seasons from all wind directions compared to warm seasons (see Figs. 5a 7a and 5d7d). In situ PM$_{2.5}$ values also show similar decrease from warm to cold seasons, especially from the pollution transport direction (i.e., 160°; see Figs. 5b 7b and 5e7e). More importantly, no clear vertical structure changes were found for aerosol observations in different seasons. One reason could be that the vertical structure of aerosols does not change for different seasons in this area, or the instruments are not sensitive enough to reveal such changes (i.e., the precision of aerosol measurements and wind data). Another reason is that there are some high background aerosols that do not depend on the wind direction. In short, Fig. 5 7 reveals that the biases between AOD and PM$_{2.5}$ data are different in different seasons. The surface to column ratio of aerosol data (see Figs. 5c 7c and f) show higher than background values from 160° directions for both cold and warm seasons. Such ratio is lower in cold seasons (91 μg/m^3 vs. 103 μg/m^3 at 70 m in cold and warm seasons, respectively)

and intersect with background conditions (green line) at 180 m (Fig. ~~5f~~7f), indicating the aerosols layers are less sensitive to winds above this height in cold seasons. More discussion and interpretation of such ratio values are provided in Sect. 5.2.

~~**45. Horizontal transport differences**~~

~~**4.1 SO₂ transport observations**~~

5 ~~Information about the wind speed in addition to wind direction could further help to characterize the pollution sources.~~

~~In this section, the SO₂ observations from Pandora and in situ instrument are binned by the wind direction and speed data at a specific wind layer from WindRASS (i.e., SO₂ data binned by wind directions using 20° bins and by wind speed using 1 m s⁻¹ bins, at a certain height). The SO₂ data are plotted using polar coordinates where the radius refers to the wind speed and angle refers to the wind direction. The color of the shading areas represents the VCD or surface~~
10 ~~concentration of SO₂. For example, Fig. 6a shows the Pandora SO₂ vertical column data displayed in such polar coordinates. The wind information for this plot was from WindRASS data at a height of 250 m, as indicated on the plot. The wind layer was chosen as both the remote sensing and in situ observations show maximum sensitivity of the SO₂ plume at this layer (see Fig. 3). Figure 6a shows the pollutants (SO₂ VCD) were transported from 130° to 190° wind directions and reached maximum values at a wind speed of about 7 m s⁻¹. Low wind speed conditions (e.g., < 4 m s⁻¹)~~
15 ~~within this direction range will have lower observed signals compared to higher wind speeds. In contrast, Fig. 6b shows the in situ observations are sensitive to similar wind directions but elevated SO₂ surface concentrations are less sensitive to the wind speed than VCDs.~~
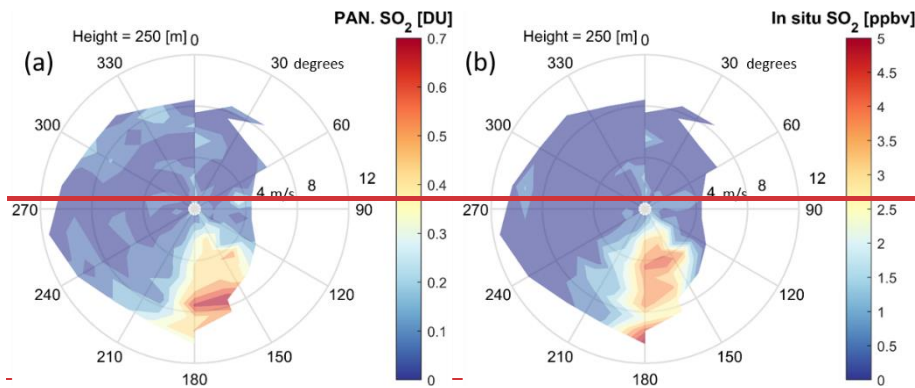

~~**Figure 6. SO₂ horizontal transport pattern resolved by wind speed and directions. SO₂ observations from (a) Pandora**~~
20 ~~**(SO₂ VCD in DU) and (b) the in situ instrument (SO₂ surface concentration in ppbv) at Oski-Otin. Wind information**~~
~~**from WindRASS data at 250 m layers where both Pandora and in situ instrument show maximum sensitivity to wind**~~

21

from the pollution sources (from 160°). The polar plot bins the SO$_2$ data (color-coded shading areas) by wind directions (angle values in degrees) and wind speed (radius values in m s^{-1}).

Both Pandora and in situ instruments show the same behaviour with wind speed: high SO$_2$ for relative higher wind speed (4–8 m s^{-1}) and low for low wind speed (<1 m s^{-1}). This is simply because there are no local SO$_2$ sources in Fort McKay. The higher the wind speed, the less time the pollutants need to travel from the source to the measurement site. Since the upgraders are about 20 km away from the observation site, fast winds would be corresponding to a transit time of about 1 hour; while slow winds would corresponding to about 6 hours. As SO$_2$ has a relatively short lifetimes in lower troposphere (of a few hours), the less time it takes to travel, the higher are the observed VCD or surface concentrations. If the wind speed is even higher (>8 m s^{-1}), the SO$_2$ signal is low again since the pollutant is spread over a larger area, while its total mass, determined by the emission rate and the lifetime, remains constant (e.g., see SO$_2$ VCD plume model from Fioletov et al., 2015).

4.2 NO$_2$ transport observations

For NO$_2$, the data were analyzed at two different wind layer heights, i.e., wind data from the 250 m layer (same as Fig. 6 which has high sensitivity to the wind direction for SO$_2$ data and remote sensing NO$_2$ data) and 60 m layer (high sensitivity for in situ NO$_2$ data, as shown in Fig. 4). In contrast to the single source direction for SO$_2$ (160°), two distinct NO$_2$ source directions were found at 40° and 160° (Fig. 7a and 7c). As shown in Fig. 2, the NO$_2$ source from 40° is related to the mining area in the North West direction of the observation site (NO$_2$ emission mainly from mining fleet). The 160° directions have NO$_2$ emissions from both stacks and mining fleet (surface emissions >50%). The in situ instrument revealed the same source directions, but with different sensitivities to wind speed and wind layers. Fig. 7b shows that the 250 m layer wind is not good enough to isolate NO$_2$ sources, if using the in situ NO$_2$ observations. When using the wind layer at 60 m, Fig. 7d shows that the in situ instrument has increased sensitivity to surface NO$_2$ at low wind speed conditions (i.e., < 4 m s^{-1}). The results confirmed that remote sensing and in situ instruments have different sensitivity to different layers of the pollutants, thus when comparing the results of their observations, extra caution

should be given to account for such differences. Note that the directions of the winds with the highest NO$_2$ values are somewhat different between the two layers that may be related to vertical wind shear.
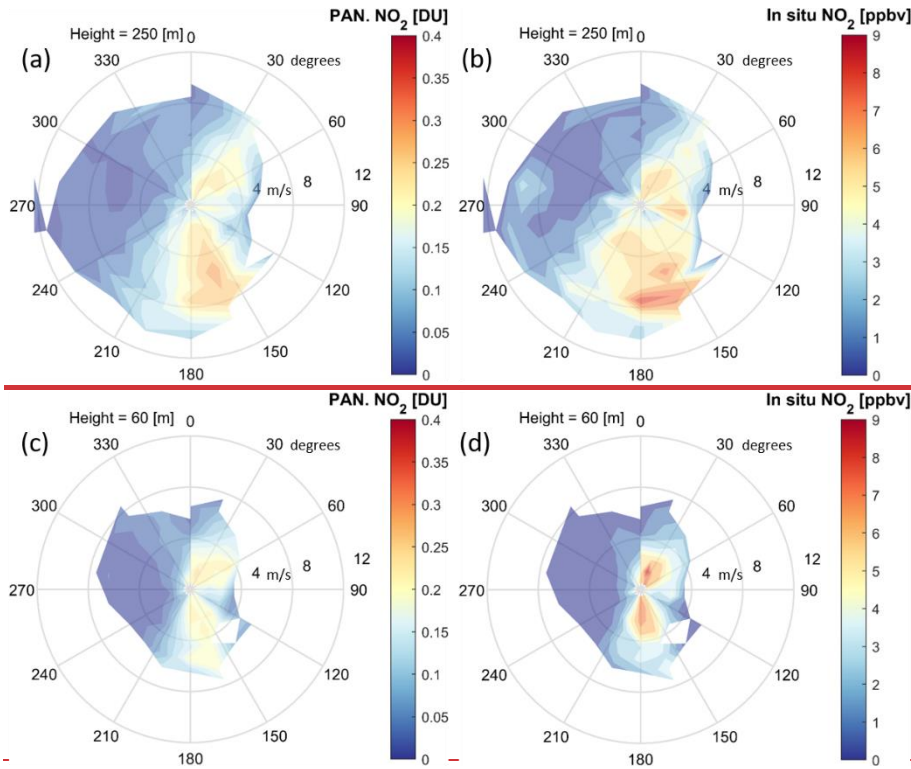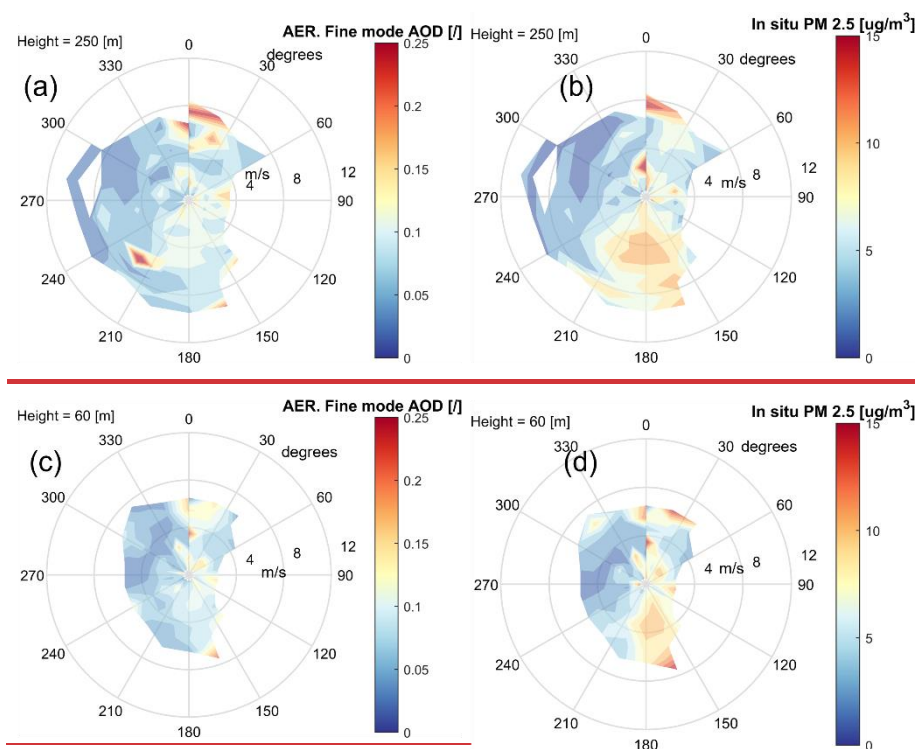
4.3 Aerosol transport observations

As illustrated in Fig. 5 and discussed in Sect. 3.3, there are larger differences between AOD and in situ measurements in determining the aerosol pollution directions. It is worth noting that there were no clear vertical structures that can be used to identify the optimal wind layers to separate and isolate potential aerosol sources. As a result, various wind layers and wind bins were examined. Not surprisingly, we did not find an optimal wind layer or wind bins that shows agreement between remote sensing and in situ measurements (see Fig. 8; which shows only warm seasons, when the aerosol loads are high). However, some general patterns can still be observed. In situ data show a clear aerosol source at 160° and other sources from the North and North East (see Fig. 8b and 8d; 250 m and 60 m wind layers, respectively), but with slightly different patterns in terms of wind speed. The source in the North-East directions can be detected in

23

high wind conditions (e.g., about 7 m s^{-1}), whereas the source in South East directions can be detected in almost all wind conditions. This could indicate different distances of the source of PM$_{2.5}$ and the observation site, i.e., the South East source is closer. It is also worth noting that remote sensing instruments revealed those two aerosol sources, e.g., Fig 8a. However, the remote sensing observations demonstrate elevated AODs only for high wind conditions. A better explanation of such difference between sunphotometer's fine mode AOD and in situ instrument's PM$_{2.5}$ observations is still needed.

Figure 8. Aerosol horizontal transport pattern resolved by wind speed and directions. Aerosol observations from (a and c) sunphotometer (fine mode aerosol optical depth, unitless) and (b and d) the in situ instrument (PM$_{2.5}$ surface concentration in µg m^{-3}) at Oski-Otin. Wind information from WindRASS data at 250 m layer (a and b) and 60 m layer (c and d). The polar plot bins the aerosol data (color-coded shading areas) by wind directions (angle values in degrees) and wind speed (radius values in m s^{-1}).

5. Reanalysis meteorological data

Sections 3 and 4 demonstrated that vertical wind profiling information could play important roles in air quality monitoring and pollution transportation studies. However, such instruments (e.g., WindRASS) only provide limited coverage spatially (not many Pandoras or other air quality monitoring instruments are co-located with wind profiling instruments) and vertically (as

24

discussed in ~~Sect. 3~~Appendix A, this WindRASS instrument only had good vertical coverage from 40 m to about 300 m above ground level (a.g.l.)). On the other hand, reanalysis meteorological data (e.g., ERA-5) have been used extensively in many research applications (e.g., Hersbach et al., 2020)~~; and~~ reanalysis wind data have quality acceptable for many applications and the advantage of good temporal coverage and global spatial coverage. For example, in our previous work, ERA-5 winds from 1000 to 900 hPa were averaged to provide wind direction and speed information to facilitate satellite validation and regional air quality monitoring (Zhao et al., 2020, 2022). However, these wind layers may not always be optimal for different conditions (i.e., different species and/or emission sources heights as illustrated in previous sections).

In this part, we present a similar analysis as Sect~~s~~. ~~3 and~~ 4, but instead of WindRASS observations, ERA-5 model level wind data are utilized (from ERA-5 model levels 100 to 137; note level 137 is the bottom/ground level). This part of the study is to: 1) verify if ERA-5 winds can distinguish the pollution vertical and horizontal transport patterns as well as WindRASS, and 2) provide knowledge on the optimal ERA-5 wind layers that can be used for satellite-based pollutant emission estimations.

5.1 Wind analysis with ERA-5 data

Figure ~~9~~8 shows the vertically resolved sensitivity analysis for SO_2 (first row), NO_2 (second row), and aerosol (third row) observations (similar to the results in Sect. ~~3~~4, but utilizing ERA-5 wind data). To make the analysis comparable to the WindRASS data, the hourly ERA-5 model level wind data were interpolated to 100 m vertical resolution. The first two columns of Fig. ~~9~~8 show the ERA-5 model results that represent the 0 m to 2000 m range (a.g.l), with only wind directions of 160° and 280°.

Figures ~~9a~~8a and b show that the SO_2 VCD and surface concentration observations show similar sensitivity to certain wind layers when ERA-5 winds are used instead of WindRASS data. For example, in warm seasons (see solid lines), both VCD and surface concentration of SO_2 show higher sensitivity to winds below 2 km; while in cold seasons, these observations of SO_2 show higher sensitivity to winds only below 0.5 km (see dashed lines). This seasonal difference was also found when using WindRASS data (see Sect. ~~3~~4.1). Note that a direct comparison between ERA-5 winds and WindRASS observations results is challenging due to limited spatial (0.25° × 0.25°, approximately, 30 km × 15 km at Fort McKay) and vertical resolution of ERA-5 data (60–90 m below 500 m compared to 10 m for WindRASS).

In Figs. ~~9a~~8a and b, one major difference between ERA-5 and WindRASS results is the maximum sensitivity height. For SO_2 VCD observations, when using WindRASS, it has maximum sensitivity to winds from 250–300 m altitude (a.g.l; see Sect. ~~3~~4.1). This could be due to the fact the WindRASS could not provide good sampling above this layer. When using ERA-5, SO_2 observations show a clear change in ~~its~~ their maximum sensitivities for wind layers from 0–1400 m in warm seasons down to 0–500 m in cold seasons. Gordon et al. (2018) and Davis et al. (2020) show the retrieved SO_2 vertical profiles from

25

MAX-DOAS and aircraft measurements with plume heights could reach 600 m to 1000 m altitude. Note that WindRASS only provides good samplings for wind layers at altitudes below 400–500 m.
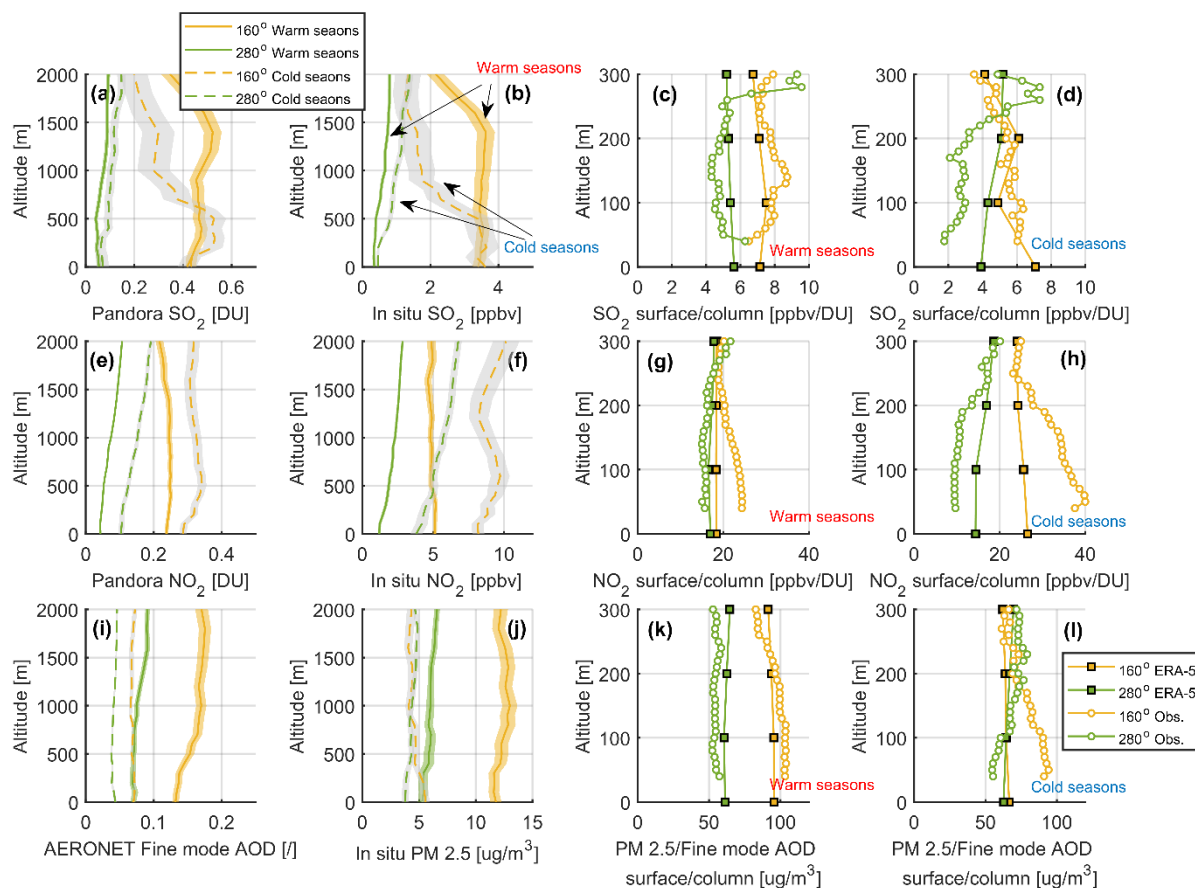

Figure 98. The mean SO₂, NO₂, and aerosol as a function of the direction of winds (only 160° and 280°) at different altitudes from Pandora and in situ instruments at Oski-Otin. Other details of this figure are the same as Fig. 35, but the wind data is from ERA-5 reanalysis data (first two columns), not the WindRASS observations. Last two columns show the surface to column ratio for selected wind directions; solid lines with square symbols use wind data from ERA-5 reanalysis, lines with circles symbols use wind data from the WindRASS observations.

For NO₂, Figs. 9e 8e and f show that the largest NO₂ source is from 160° while the clean air is from 280° wind directions, consistent with findings in Sect. 34.2. For cold seasons, the NO₂ sensitivity height from 160° directions is consistent with the SO₂ results, indicating they both emitted from similar high stacks from these directions.

When using ERA-5 winds, the results for aerosol are also generally consistent with previous findings in Sect. 34.3. Figures 9i 8i and j both confirm that there is a PM₂.₅ source from the 160° direction. Figures 9i 8i and j show that this aerosol

source can be better identified, if using winds from 500–1500 m layers. This feature is also partially reflected in Fig. ~~5a~~ 7a but not as clear as Fig. ~~9i~~ 8i due to the low data availability of WindRASS for higher altitudes. In general, Figs. ~~9i~~ 8i and j shows both AOD and $PM_{2.5}$ data do not have strong changes in their vertical sensitivity to different layers of winds~~;~~, i.e., we find no clear "plume" heights changes for aerosol, in contrast to what we saw for SO_2 and NO_2 results. This result indicates that the aerosol is better vertically mixed than SO_2 and NO_2 emissions from high stacks. More details of horizontal transport differences when using ERA-5 winds are shown in Appendix ~~B~~C.

Regarding the surface to column ratios (0–300 m), the last two columns of Fig. ~~9~~ 8 show a general agreement between the results based on WindRASS (see circles symbols) and reanalysis (see square symbols) data (i.e., the ratios are typically higher from polluted directions than clean air directions), although the altitudinal dependence has some differences. For SO_2, the higher surface to column ratios from 160° directions in cold seasons (Fig. ~~9d~~8d) ~~is~~ are generally preserved when using ERA-5 winds. For example, in cold seasons, the highest surface to column ratios from 160° directions ~~is~~ are 7 ppbv DU^{-1} (at 0 m altitude) and 6 ppbv DU^{-1} (at 90 m altitude), for using ERA-5 and WindRASS measurements respectively. Overall, for SO_2, ERA-5 results generally preserved the features of ratio changes. For NO_2, the higher pollutant to clean ratio differences are found in cold seasons (Figs. ~~9g~~8g-h), which is similar to the results when using WindRASS measurements. However, the larger discrepancy is found near the surface, where WindRASS results show higher ratios from 160° directions. These differences are mainly due to the coarse spatial and vertical resolution of ERA-5 data (i.e., only four data points for this 0–300 m range) and sampling issues with WindRASS measurements. The results for aerosol are similar to NO_2, and has better agreement in warm seasons.

5.2 Boundary layer height effect on the column to surface ratio

As shown in Sects. ~~3~~4 and 5.1, for tropospheric pollutants, the surface to column concentration ratio can reveal some information about the vertical distribution. One important finding is that such ratios change with wind directions and also has seasonal patterns (e.g., see Fig. ~~9~~8). The boundary layer height data from the lidar observations could provide critical information to help further interpret the difference between the vertical column and surface observations.

To better illustrate the effect of low BLH conditions on the SO_2 plume's vertical distribution, in this section, we plotted the column to surface ratio. For example, Fig. ~~10~~ 9 shows the column to surface ratio binned by boundary layer height in warm seasons. Here the column values (SO_2 and NO_2 VCD, in the unit of DU; AOD is unitless) are from remote sensing observations, while SO_2, NO_2, and $PM_{2.5}$ surface concentration values (SO_2 and NO_2 in the unit of ppbv; $PM_{2.5}$ in unit of µg m^{-3}) are from in situ measurements and the BLH values are from lidar observations. Figures ~~10a~~9a, d, and g show the boxplot of all observations; Figs. ~~10b~~9b, e, and h show the results representing observations with winds from the second-largest NO_2 sources (i.e., winds from 40° ± 30°; facilities of Syncrude, Shell Canada Limited, Canadian Natural Resources Limited, and Imperial Oil Resources); Fig. ~~10c~~9c, f, and i represent winds from the largest SO_2 and NO_2 sources (i.e., winds from 160° ±

27

30°; facilities of Suncor and Syncrude). The results clearly show that, for the SO_2 plume from upgraders (see Fig. ~~10c~~9c), the SO_2 column to surface ratio is a monotonic declining function of ~~negatively correlated to~~ BLH (with a Spearman correlation coefficient of -0.83). In other words, in low BLH conditions, surface in situ and remote sensing observations will likely show more differences for such elevated plumes.
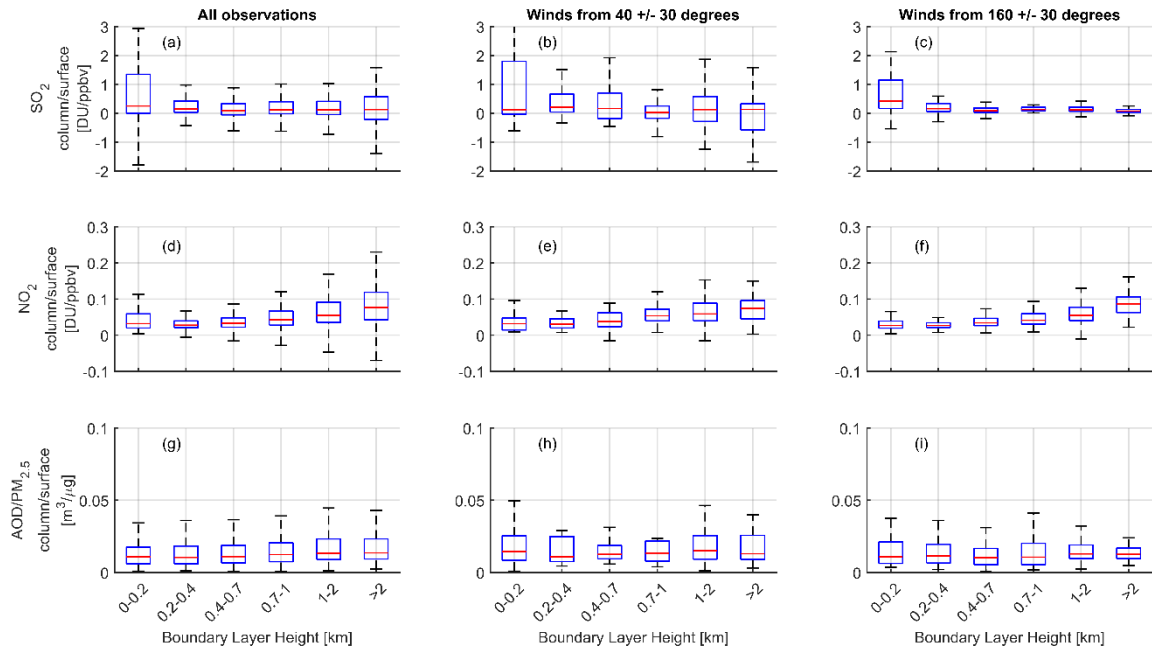
5

Figure ~~10~~9. Boxplot of SO_2, NO_2, and $AOD/PM_{2.5}$ column to surface ratio binned by boundary layer height in warm seasons. Panel (a), (d), and (g) show all observations; panels (b), (e), and (h) show observations with winds from $40° \pm 30°$ directions; panels (c), (f), and (i) show observations with winds from $40° \pm 30°$ directions. For SO_2 and AOD, the wind data is from WindRASS observations at 250 m altitudes. For NO_2, the wind data is from WindRASS observations at 60 m altitudes. The boundary layer height is measured with lidar. The SO_2 and NO_2 column observations are from Pandora, AOD observations are from sunphometer, and all surface concentrations are from in situ instrument. On each box, the red central mark indicates the median, and the bottom and top edges of the blue box indicate the 25th and 75th percentiles, respectively. The black whiskers extend to the most extreme data points not considered outliers.

15   In contrast, a similar analysis for NO_2 observations shows different features (see Figs. ~~10d~~9d-f). This time, as NO_2 has two major source directions (40° and 160° directions), Figs. ~~10e~~9e and f show clear and similar column to surface ratio patterns, i.e., this ratio is positively correlated with BLH (with a Spearman correlation coefficient of 0.94 and 1). This result indicates that the NO_2 plumes have different vertical distributions than SO_2 plumes (note that, different than SO_2 emissions from high stacks, the truck fleet in the mining area is one of the main NO_x emission sources).
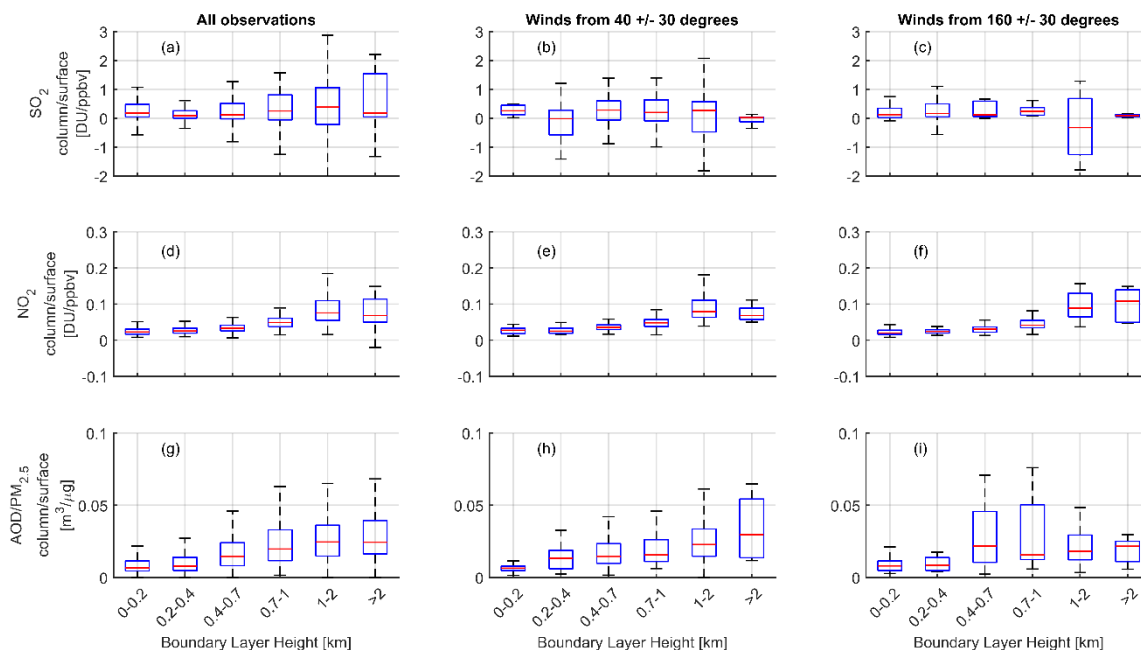
28

Figure 1110. Boxplot of SO₂, NO₂, and AOD/PM₂.₅ column to surface ratio binned by boundary layer height in cold seasons. Panel (a), (d), and (g) show all observations; panels (b), (e), and (h) show observations with winds from 40° ± 30° directions; panels (c), (f), and (i) show observations with winds from 40° ± 30° directions. For SO₂ and AOD, the wind data is from WindRASS observations at 250 m altitudes. For NO₂, the wind data is from WindRASS observations at 60 m altitudes. The boundary layer height is measured with lidar. The SO₂ and NO₂ column observations are from Pandora, AOD observations are from sunphotometer, and all surface concentrations are from in situ instrument.

When performing the same analysis for AOD (from sunphotometer) and PM₂.₅ (from in situ measurements) observations, the results are not clear in warm seasons (see Figs. 10g9g-i), similar as in Sects. 34.3 and 4.3. I.e., no simple column-to-surface ratio correlations were found from 40° and 160° directions. Such results indicate the aerosol from two pollution sources (40° and 160° directions) are well mixed, consistent with findings in Sect. 34.3 (i.e., no vertical sensitivity changes when using different wind layers). However, in cold seasons, there is a positive correlation between the AOD/PM₂.₅ ratio to BLH data from 40° direction (see Figs. 11h10h; with a Spearman correlation coefficient of 1). Thus, in cold seasons, from this direction, the aerosol loads are closer to the surface than vertically mixed. A table of detailed correlation coefficient values for Figs. 9 and 10 are provided in Appendix C.

However, as discussed, WindRASS or lidar observations are not typically available for Pandora or sunphotometer sites. As a result, such pollutants' vertical distribution information is hidden within Pandora and sunphotmeter observed data. We tested by replacing WindRASS and lidar observations with ERA-5 modelled results (wind profiles and BLH), and repeated the analysis shown above. The results show ERA-5 data could also assist the work in terms of separated pollutants' signal from different sources (see Figs. B2C2, and B3C3, and Table C1). In general, besides wind conditions (directions and speed)

and BLH, there could be other meteorological factors played roles in describe the difference between in situ and remote sensing measurements. For example, we examined combined meteorological factor, such as the ventilation coefficient (BLH × wind speed), which is also referred to as the normalized dilution rate (e.g., Gani et al., 2019). However, no improvement compared to BLH-based results was found, likely due to the complexity of the pollution source distribution. More detailed high-resolution modelling work is needed to further understand the meteorological impacts to local observations.

6. Integration period differences

In contrast to in situ instruments that can obtain 24 hr continuous observations, passive remote sensing instruments (i.e., use the sun as a light source) can only deliver data when direct solar light can reach the instruments. Figure 12 shows the coincident observations from remote sensing (blue solid lines with error bars) and in situ (red solid lines with error bars) observations that have been averaged by the hour (local standard time). Both SO_2 and NO_2 data show good agreement in variation patterns except early morning. The prominent discrepancy in the morning could be related to larger changes in the mixing layer height and related vertical mixing conditions. For example, in cold seasons, with increased mixing layer height and vertical dynamics from the morning to noon, in situ SO_2 shows a strong increase from 0.40 ppbv at 6 am to 1.18 ppbv at 10 am (see Fig. 12). In contrast, the Pandora observations show an opposite decreasing trend; the VCD of SO_2 decreased from 0.32 DU at 6 am to 0.01 DU at 10 am. As discussed before, Pandora can sample the entire vertical column of SO_2 molecules, thus the increase of surface SO_2 concentration (from less than 0.5 ppbv at 6 LST to almost 1.5 ppbv at 10 SLT) in the morning (see Fig. 12b, in the warm seasons) is not due to increased emission (SO_2 VCD values are stable from 6 to 10 LST) but due to vertical mixing. Better vertical mixing
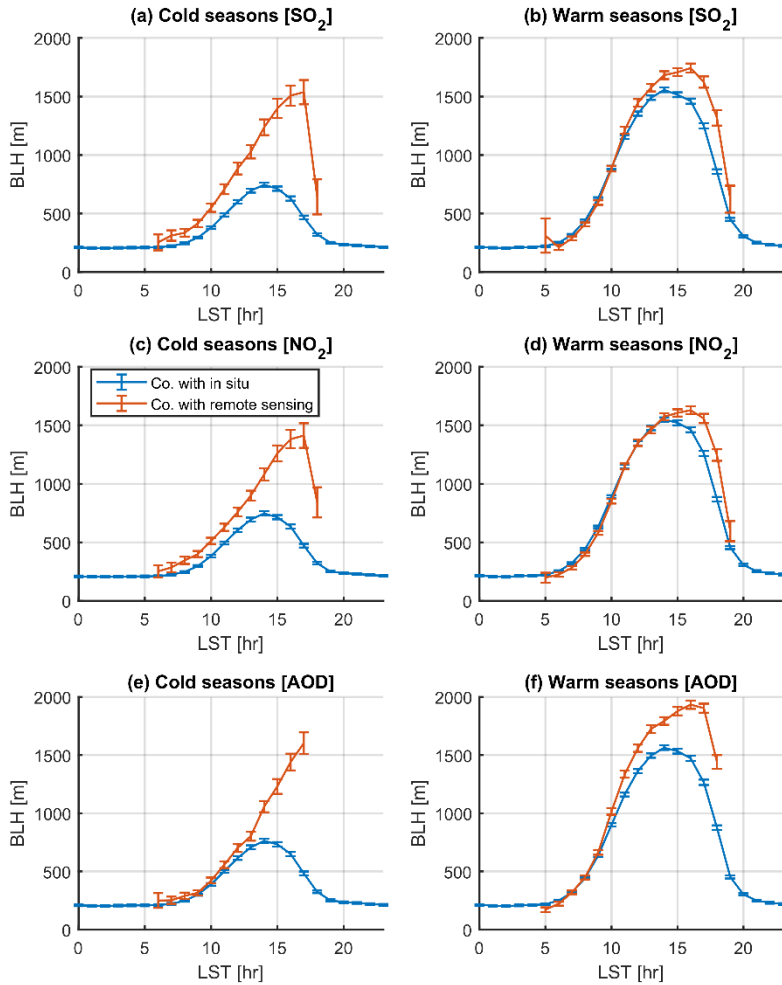
sensing observations; dashed red lines show all in situ measurements. Results from warm seasons are shown in panels (a), (c), and (e); results from cold seasons are shown in panels (b), (d), and (f).

The conditions for NO_2 are similar to SO_2 but show stronger indications from photochemistry, i.e., generally decreased values of NO_2 from morning to evening. Moreover, as there are strong NO_2 sources near ground level, even the VCD are stable from 8 to 15 LST (e.g., see Figs. 12 b), the surface value is keep decreasing. For aerosol comparison, both AOD and $PM_{2.5}$ show clear U-shape changes over the day in warm seasons (see Fig. 12f). However, in the afternoons of cold seasons, $PM_{2.5}$ shows a decreasing trend, while AOD has an increasing trend (see Fig. 12e). Thus, without detailed meteorological information (e.g., BLH and vertically resolved wind information), there is no surprise that we could not find an easy and clear correlation between remote sensing and in situ observations.

In addition to data sampled at the time of measurements by remote sensing instruments, results based on all in situ measurements are plotted in Fig. 12 as red dash lines. When comparing red dash lines with red solid lines, the results from Fig. 12 shows interesting and prominent features, i.e., when pairing in situ data with remote sensing data, sometimes, the diurnal patterns of in situ measurements are changed (e.g., see Fig. 12e, the different variations of the red solid and red dashed lines). The cause of such changes is due to the "sampling bias" from remote sensing measurements that are available under unobscured sun conditions only; in situ data has no major gaps. Although the local emissions conditions might not be different in sunny or rainy days, the difference in meteorological conditions can affect the pollutants monitoring results. For example, Fig. 13 shows the ERA-5 boundary layer height data binned by hours of local standard time. The BLH data that coincident with in situ SO_2 measurements show clear seasonal difference (see blue lines in Figs. 13a and b); in cold seasons, the highest BLH data only reach 750 m, while in warm seasons it can reach 1500 m. The diurnal variations of BLH data show bell curves as in situ instruments performs sampling 24 hr per day in all weather conditions. However, the BLH data that coincident with remote sensing SO_2 measurements (see red lines in Figs. 13a and b) show more skewed shapes, i.e., higher BLH values in afternoons. Especially, in the wintertime (Fig. 13a), BLH data that coincident with remote sensing observations shows a much stronger increasing from 10 to 16 LTS than its counterpart that coincident with in situ measurements. Similar features can be seen for NO_2 and aerosol data. Thus, it is clear that remote sensing observations are biased to high BLH conditions, especially in afternoons. These results also explain why, when coincident with remote sensing observations, in situ diurnal patterns changed (see Fig. 12). For example, in cold seasons at 17 LST, by pairing $PM_{2.5}$ data with AOD data, the corresponding BLH value increased from 500 m to 1500 m (see Figs. 13e) and thus the $PM_{2.5}$ values changed from 6.0 µg m^{-3} to 2.9 µg m^{-3} (see Fig. 12e). Such variation in diurnal patterns is not obvious in warm seasons, due to less BLH changes (due to coincident selection with remote sensing instrument) than cold seasons. For instance, by selecting coincident measurements, measured NO_2 surface values dropped from 11.3 pptv to 2.5 pptv in cold seasons at 17 LST (Fig. 12e); while the corresponding values only dropped from 2.5 pptv to 2.0 pptv, in warm seasons (Fig. 12d). In other words, the sampling biases between remote sensing and in situ data are worse in cold seasons than warm seasons. When direct comparing coincident remote sensing and in situ observations, such weather condition biased sampling would not easily been revealed. However, this clear-sky bias could lead to significant differences in long-term trend analysis.

In short, similar to findings in Sects. 3 to 5, Figs. 12 and 13 show that depending on the height of the emission sources, boundary layer dynamics can play important roles in the sampling differences between remote sensing and in situ instruments. Modelling of boundary layer conditions is also known to be a major difficulty for air quality modelling work (e.g., Zhao et al., 2019). This indicates a great need for improved boundary layer height observations from other remote sensing instruments (Szykman et al., 2019). This issue could be more prominent if the remote sensing air quality

32

33

7~~6~~. Conclusion

5   This work analyzed the sampling differences (of SO_2, NO_2, and aerosol) between remote sensing and in situ instruments in the ~~Canadian~~ Athabasca oil sands region, in terms of vertical, horizontal, and temporal dependency on ~~meteorological conditions~~ ~~(~~wind speed, directions, altitude, and BLH~~)~~. Results show that depending on the height of emission sources, remote sensing and in situ instruments could sample different parts of pollutant plumes, due to their different vertical sensitivity ranges. For elevated pollutants (e.g., SO_2 emission via high stacks), both remote sensing and in situ ~~instruments~~ data show strong

10   dependence on wind information above stack height level (i.e., around 250 m for this case). The magnitude of the SO_2 VCD and surface concentrations reach their maximum for winds from $160° \pm 30°$ directions at 200–300 m altitudes ~~(which is about~~ ~~38% and 27% higher than the value for winds from the same directions but of near surface winds, respectively)~~. Note that, for warm and cold seasons, the median values of BLH are 390 m and 208 m, respectively. In contrast, the NO_2 emissions from $160° \pm 30°$ directions are from both high stacks and the mining fleets. As a result, NO_2 VCD shows a more uniform sensitivity

15   to winds from near surface to up to 300 m (peak value at 260–290 m altitude), while in situ measured NO_2 surface concentrations show a strong sensitivity to near-surface winds (peak value at 60–70 m altitude). In cold seasons, the NO_2 surface to column ratio from $160°$ direction changes from 39 ppbv/DU at 70 m to 28 ppbv/DU at 200 m. Such key differences indicate the challenges in applying remote sensing observations in "breathing-height" air quality applications. In other words, although VCDs measured by remote sensing instruments represent integrated pollutants that are sensitive to both surface and

20   upper levels, the observations could not easily be separated or linked to localized surface value. On the other hand, while elevated air pollutants cannot be monitored at the surface via in situ measurements, they can still be captured by remote sensing instruments. Thus, these VCD observations could be more useful in quantifying total emissions than surface observations for such emission sources. Also, it is worth noting that elevated air pollutants, which ~~that~~ do not affect the air quality immediately as they are above ground level, could still pose a health risk further downwind as the pollutants will eventually reach the

25   surface via vertical mixing. Thus, remote sensing VCD observations could represent air quality conditions for a much larger area than localized surface in situ measurements.

~~The horizontal transport sampling differences show that local sources have the largest impact on observations when the wind speed is low and the pollutants are not transported far from the source (as in the case of some NO_2 emissions). For elevated sources (e.g., SO_2 emitted from high stacks), the moderate wind is substantial to bring the pollutant to the measurement~~

34

site. Compared to in situ instruments, remote sensing observations are more sensitive to higher wind speed conditions, i.e., transported pollutants.

Comparing AOD and surface $PM_{2.5}$ measurements is the most challenging workcomplicated, as their vertical and horizontal patterns are not very alike. Such larger differences are expected as these two measurements (AOD and $PM_{2.5}$) do not necessarily represent the same matter, not only due to the different sampling area but also due to large seasonal cycle and high background. Comparisons are easier for e.g. SO_2, where remote sensing measured VCD (in DU) represents the SO_2 within the entire vertical column; in situ measured surface concentration (in ppbv) represents the portion of SO_2 within the air mass near the surface. Although many studies exist that directly compare these two measurements (AOD and $PM_{2.5}$) and often reveal positive correlations, there are no simple methods exists to directly connect or convert them (e.g., only empirical methods or via modelling means). In general, due to the complex nature of PM, the conversion from $PM_{2.5}$ to AOD (or vice versa) is not straightforward. Here we show that linking these two measurements could be even more complicated, as they have more sampling differences than observations of trace gases. On the positive side, both remote sensing and in situ observations show consistent uniform sensitivities to the wind speed and direction from near surface to 300 m altitude, indicating the aerosol loads in this region are more uniformly mixed than SO_2 and NO_2.

This analysis also shows that ERA-5 model level winds produce results similar to those for direct wind measurements by WindRASS at this location and, therefore, can be a good tool to support ground-based remote sensing research to identify pollutant sources' directions and even their vertical structures. Using measured wind profiles and BLH, the work demonstrated that the column to surface ratio of pollutants could show positive or negative correlations with boundary layer heights, depending on the height of emission sources. Further results show replacing measured wind profiles and BLH by ERA-5 data could also preserve these features. Thus, the boundary layer height and wind profile data from these ERA-5 data also can be utilized to reveal pollutants' vertical distribution and mixing conditions, which can be used as critical information when converting remote sensing column data to surface values. Current results also suggest that, for wind-rotation SO_2 or NO_2 emission models (e.g., Fioletov et al. (2016, 2022)) and wind-rotation satellite data validation method (Park et al., 2022; Zhao et al., 2020), different layers of ERA-5 winds should be averaged, and some seasonal changes might be considered to improve the results.

This analysis of surface to column ratios also shows that the column values cannot be converted to surface by just one value of the ratio. Depending on the wind direction (and season), the ratio for directions related to the pollution sources could be a factor of two larger than these from "clean" directions.

The overall outcome of this work is to reveal and analyse analyze the fundamental sampling differences between remote sensing and in situ observations via utilizing vertical wind observations and boundary layer conditions. Other aspects, such as sampling areas and clear-sky bias still need further investigation. In particular, as remote sensing instruments discussed here are sunlight instruments and their observations are clear-sky biased, these could lead to differences in long-term trend

analysis done with in situ and remote sensing instruments alone. These ground-based remote sensing air quality observations (e.g., Pandora spectrometer and CIMEL sunphotometer) cannot replace surface in situ monitoring, but can play a key role in linking satellite air quality observations and surface in situ measurements.

References

Barkley, M. P., González Abad, G., Kurosu, T. P., Spurr, R., Torbatian, S., and Lerot, C.: OMI air-quality monitoring over the Middle East, Atmos. Chem. Phys., 17, 4687–4709, https://doi.org/10.5194/acp-17-4687-2017, 2017.

5 Davis, Z. Y. W., Frieß, U., Strawbridge, K. B., Aggarwaal, M., Baray, S., Schnitzler, E. G., Lobo, A., Fioletov, V. E., Abboud, I., McLinden, C. A., Whiteway, J., Willis, M. D., Lee, A. K. Y., Brook, J., Olfert, J., O'Brien, J., Staebler, R., Osthoff, H. D., Mihele, C., and McLaren, R.: Validation of MAX-DOAS retrievals of aerosol extinction, SO_2, and NO_2 through comparison with lidar, sun photometer, active DOAS, and aircraft measurements in the Athabasca oil sands region, Atmos. Meas. Tech., 13, 1129–1155, https://doi.org/10.5194/amt-13-1129-2020, 2020.

10 Dieudonné, E., Ravetta, F., Pelon, J., Goutail, F., and Pommereau, J.-P.: Linking NO_2 surface concentration and integrated content in the urban developed atmospheric boundary layer, Geophys. Res. Lett., 40, 1247–1251, https://doi.org/10.1002/grl.50242, 2013.

Duncan, B. N., Lamsal, L. N., Thompson, A. M., Yoshida, Y., Lu, Z., Streets, D. G., Hurwitz, M. M., and Pickering, K. E.: A space-based, high-resolution view of notable changes in urban NOx pollution around the world (2005–2014), J. Geophys. Res.,
15 121, 976–996, https://doi.org/10.1002/2015JD024121, 2016.

Fioletov, V., McLinden, C. A., Griffin, D., Theys, N., Loyola, D. G., Hedelt, P., Krotkov, N. A., and Li, C.: Anthropogenic and volcanic point source SO_2 emissions derived from TROPOMI on board Sentinel-5 Precursor: first results, Atmos. Chem. Phys., 20, 5591–5607, https://doi.org/10.5194/acp-20-5591-2020, 2020.

Fioletov, V., McLinden, C. A., Griffin, D., Krotkov, N., Liu, F., and Eskes, H.: Quantifying urban, industrial, and background
20 changes in NO_2 during the COVID-19 lockdown period based on TROPOMI satellite observations, Atmos. Chem. Phys., 22, 4201–4236, https://doi.org/10.5194/acp-22-4201-2022, 2022.

Fioletov, V. E., McLinden, C. A., Krotkov, N., Moran, M. D., and Yang, K.: Estimation of SO_2 emissions using OMI retrievals, Geophys. Res. Lett., 38, L21811, https://doi.org/10.1029/2011GL049402, 2011.

Fioletov, V. E., McLinden, C. A., Krotkov, N., and Li, C.: Lifetimes and emissions of SO_2 from point sources estimated from
25 OMI, Geophys. Res. Lett., 42, 1969–1976, https://doi.org/10.1002/2015GL063148, 2015.

Fioletov, V. E., McLinden, C. A., Cede, A., Davies, J., Mihele, C., Netcheva, S., Li, S.-M., and O'Brien, J.: Sulfur dioxide (SO_2) vertical column density measurements by Pandora spectrometer over the Canadian oil sands, Atmos. Meas. Tech., 9, 2961–2976, https://doi.org/10.5194/amt-9-2961-2016, 2016.

de Foy, B., Lu, Z., Streets, D. G., Lamsal, L. N., and Duncan, B. N.: Estimates of power plant NOx emissions and lifetimes
30 from OMI NO_2 satellite retrievals, Atmos. Environ., 116, 1–11, https://doi.org/10.1016/j.atmosenv.2015.05.056, 2015.

Gani, S., Bhandari, S., Seraj, S., Wang, D. S., Patel, K., Soni, P., Arub, Z., Habib, G., Hildebrandt Ruiz, L., and Apte, J. S.: Submicron aerosol composition in the world's most polluted megacity: the Delhi Aerosol Supersite study, Atmos. Chem. Phys., 19, 6843–6859, https://doi.org/10.5194/acp-19-6843-2019, 2019.

Gordon, M., Makar, P. A., Staebler, R. M., Zhang, J., Akingunola, A., Gong, W., and Li, S.-M.: A comparison of plume rise algorithms to stack plume measurements in the Athabasca oil sands, Atmos. Chem. Phys., 18, 14695–14714, https://doi.org/10.5194/acp-18-14695-2018, 2018.

Herman, J., Cede, A., Spinei, E., Mount, G., Tzortziou, M., and Abuhassan, N.: NO_2 column amounts from ground-based Pandora and MFDOAS spectrometers using the direct-sun DOAS technique: Intercomparisons and application to OMI validation, J. Geophys. Res., 114, D13307, https://doi.org/10.1029/2009JD011848, 2009.

Herman, J., Evans, R., Cede, A., Abuhassan, N., Petropavlovskikh, I., and McConville, G.: Comparison of ozone retrievals from the Pandora spectrometer system and Dobson spectrophotometer in Boulder, Colorado, Atmos. Meas. Tech., 8, 3407–3418, https://doi.org/10.5194/amt-8-3407-2015, 2015.

Hersbach, H., Bell, B., Berrisford, P., Hirahara, S., Horányi, A., Muñoz-Sabater, J., Nicolas, J., Peubey, C., Radu, R., Schepers, D., Simmons, A., Soci, C., Abdalla, S., Abellan, X., Balsamo, G., Bechtold, P., Biavati, G., Bidlot, J., Bonavita, M., De Chiara, G., Dahlgren, P., Dee, D., Diamantakis, M., Dragani, R., Flemming, J., Forbes, R., Fuentes, M., Geer, A., Haimberger, L., Healy, S., Hogan, R. J., Hólm, E., Janisková, M., Keeley, S., Laloyaux, P., Lopez, P., Lupu, C., Radnoti, G., de Rosnay, P., Rozum, I., Vamborg, F., Villaume, S., and Thépaut, J.-N.: The ERA5 global reanalysis, Quarterly Journal of the Royal Meteorological Society, 146, 1999–2049, https://doi.org/10.1002/qj.3803, 2020.

Holben, B. N., Tanré, D., Smirnov, A., Eck, T. F., Slutsker, I., Abuhassan, N., Newcomb, W. W., Schafer, J. S., Chatenet, B., Lavenu, F., Kaufman, Y. J., Castle, J. V., Setzer, A., Markham, B., Clark, D., Frouin, R., Halthore, R., Karneli, A., O'Neill, N. T., Pietras, C., Pinker, R. T., Voss, K., and Zibordi, G.: An emerging ground-based aerosol climatology: Aerosol optical depth from AERONET, J. Geophys. Res., 106, 12067–12097, https://doi.org/10.1029/2001JD900014, 2001.

Jeong, U., Tsay, S.-C., Giles, D. M., Holben, B. N., Swap, R. J., Abuhassan, N., and Herman, J. R.: The SMART-s Trace Gas and Aerosol Inversions: I. Algorithm Theoretical Basis for Column Property Retrievals, J. Geophys. Res., 125, e2019JD032088, https://doi.org/10.1029/2019JD032088, 2020.

Judd, L. M., Al-Saadi, J. A., Szykman, J. J., Valin, L. C., Janz, S. J., Kowalewski, M. G., Eskes, H. J., Veefkind, J. P., Cede, A., Mueller, M., Gebetsberger, M., Swap, R., Pierce, R. B., Nowlan, C. R., Abad, G. G., Nehrir, A., and Williams, D.: Evaluating Sentinel-5P TROPOMI tropospheric NO_2 column densities with airborne and Pandora spectrometers near New York City and Long Island Sound, Atmos. Meas. Tech., 13, 6113–6140, https://doi.org/10.5194/amt-13-6113-2020, 2020.

Kelly, E. N., Schindler, D. W., Hodson, P. V., Short, J. W., Radmanovich, R., and Nielsen, C. C.: Oil sands development contributes elements toxic at low concentrations to the Athabasca River and its tributaries, PNAS, 107, 16178–16183, https://doi.org/10.1073/pnas.1008754107, 2010.

Kim, J., Jeong, U., Ahn, M.-H., Kim, J. H., Park, R. J., Lee, H., Song, C. H., Choi, Y.-S., Lee, K.-H., Yoo, J.-M., Jeong, M.-J., Park, S. K., Lee, K.-M., Song, C.-K., Kim, S.-W., Kim, Y. J., Kim, S.-W., Kim, M., Go, S., Liu, X., Chance, K., Miller, C. C., Al-Saadi, J., Veihelmann, B., Bhartia, P. K., Torres, O., Abad, G. G., Haffner, D. P., Ko, D. H., Lee, S. H., Woo, J.-H., Chong, H., Park, S. S., Nicks, D., Choi, W. J., Moon, K.-J., Cho, A., Yoon, J., Kim, S., Hong, H., Lee, K., Lee, H., Lee, S., Choi, M., Veefkind, P., Levelt, P. F., Edwards, D. P., Kang, M., Eo, M., Bak, J., Baek, K., Kwon, H.-A., Yang, J., Park, J., Han, K. M., Kim, B.-R., Shin, H.-W., Choi, H., Lee, E., Chong, J., Cha, Y., Koo, J.-H., Irie, H., Hayashida, S., Kasai, Y., Kanaya, Y., Liu, C., Lin, J., Crawford, J. H., Carmichael, G. R., Newchurch, M. J., Lefer, B. L., Herman, J. R., Swap, R. J., Lau, A. K. H., Kurosu, T. P., Jaross, G., Ahlers, B., Dobber, M., McElroy, C. T., and Choi, Y.: New Era of Air Quality Monitoring from Space: Geostationary Environment Monitoring Spectrometer (GEMS), B. Am. Meteorol. Soc., 101, E1–E22, https://doi.org/10.1175/BAMS-D-18-0013.1, 2020.

Knepp, T., Pippin, M., Crawford, J., Chen, G., Szykman, J., Long, R., Cowen, L., Cede, A., Abuhassan, N., Herman, J., Delgado, R., Compton, J., Berkoff, T., Fishman, J., Martins, D., Stauffer, R., Thompson, A. M., Weinheimer, A., Knapp, D., Montzka, D., Lenschow, D., and Neil, D.: Estimating surface NO_2 and SO_2 mixing ratios from fast-response total column observations and potential application to geostationary missions, J. Atmos. Chem., 72, 261–286, https://doi.org/10.1007/s10874-013-9257-6, 2015.

Kollonige, D. E., Thompson, A. M., Josipovic, M., Tzortziou, M., Beukes, J. P., Burger, R., Martins, D. K., Zyl, P. G. van, Vakkari, V., and Laakso, L.: OMI Satellite and Ground-Based Pandora Observations and Their Application to Surface NO_2 Estimations at Terrestrial and Marine Sites, J. Geophys. Res., 123, 1441–1459, https://doi.org/10.1002/2017JD026518, 2017.

Kreher, K., Van Roozendael, M., Hendrick, F., Apituley, A., Dimitropoulou, E., Frieß, U., Richter, A., Wagner, T., Lampel, J., Abuhassan, N., Ang, L., Anguas, M., Bais, A., Benavent, N., Bösch, T., Bognar, K., Borovski, A., Bruchkouski, I., Cede, A., Chan, K. L., Donner, S., Drosoglou, T., Fayt, C., Finkenzeller, H., Garcia-Nieto, D., Gielen, C., Gómez-Martín, L., Hao, N., Henzing, B., Herman, J. R., Hermans, C., Hoque, S., Irie, H., Jin, J., Johnston, P., Khayyam Butt, J., Khokhar, F., Koenig, T. K., Kuhn, J., Kumar, V., Liu, C., Ma, J., Merlaud, A., Mishra, A. K., Müller, M., Navarro-Comas, M., Ostendorf, M., Pazmino, A., Peters, E., Pinardi, G., Pinharanda, M., Piters, A., Platt, U., Postylyakov, O., Prados-Roman, C., Puentedura, O., Querel, R., Saiz-Lopez, A., Schönhardt, A., Schreier, S. F., Seyler, A., Sinha, V., Spinei, E., Strong, K., Tack, F., Tian, X., Tiefengraber, M., Tirpitz, J.-L., van Gent, J., Volkamer, R., Vrekoussis, M., Wang, S., Wang, Z., Wenig, M., Wittrock, F., Xie, P. H., Xu, J., Yela, M., Zhang, C., and Zhao, X.: Intercomparison of NO_2, O_4, O_3 and HCHO slant column measurements by MAX-DOAS and zenith-sky UV–visible spectrometers during CINDI-2, Atmos. Meas. Tech., 13, 2169–2208, https://doi.org/10.5194/amt-13-2169-2020, 2020.

Krotkov, N. A., McLinden, C. A., Li, C., Lamsal, L. N., Celarier, E. A., Marchenko, S. V., Swartz, W. H., Bucsela, E. J., Joiner, J., Duncan, B. N., Boersma, K. F., Veefkind, J. P., Levelt, P. F., Fioletov, V. E., Dickerson, R. R., He, H., Lu, Z., and Streets, D. G.: Aura OMI observations of regional SO_2 and NO_2 pollution changes from 2005 to 2015, Atmos. Chem. Phys., 16, 4605–4629, https://doi.org/10.5194/acp-16-4605-2016, 2016.

Liu, F., Beirle, S., Zhang, Q., van der A, R. J., Zheng, B., Tong, D., and He, K.: NO_x emission trends over Chinese cities estimated from OMI observations during 2005 to 2015, Atmos. Chem. Phys., 17, 9261–9275, https://doi.org/10.5194/acp-17-9261-2017, 2017.

Liu, S., Valks, P., Beirle, S., and Loyola, D. G.: Nitrogen dioxide decline and rebound observed by GOME-2 and TROPOMI during COVID-19 pandemic, Air Qual Atmos Health, 14, 1737–1755, https://doi.org/10.1007/s11869-021-01046-2, 2021.

Lu, Z., Streets, D. G., de Foy, B., Lamsal, L. N., Duncan, B. N., and Xing, J.: Emissions of nitrogen oxides from US urban areas: estimation from Ozone Monitoring Instrument retrievals for 2005–2014, Atmos. Chem. Phys., 15, 10367–10383, https://doi.org/10.5194/acp-15-10367-2015, 2015.

McLinden, C. A., Fioletov, V., Boersma, K. F., Krotkov, N., Sioris, C. E., Veefkind, J. P., and Yang, K.: Air quality over the Canadian oil sands: A first assessment using satellite observations, Geophys. Res. Lett., 39, https://doi.org/10.1029/2011GL050273, 2012.

McLinden, C. A., Fioletov, V., Boersma, K. F., Kharol, S. K., Krotkov, N., Lamsal, L., Makar, P. A., Martin, R. V., Veefkind, J. P., and Yang, K.: Improved satellite retrievals of NO_2 and SO_2 over the Canadian oil sands and comparisons with surface measurements, Atmos. Chem. Phys., 14, 3637–3656, https://doi.org/10.5194/acp-14-3637-2014, 2014.

McLinden, C. A., Fioletov, V., Krotkov, N. A., Li, C., Boersma, K. F., and Adams, C.: A Decade of Change in NO_2 and SO_2 over the Canadian Oil Sands As Seen from Space, Environ. Sci. Technol., 50, 331–337, https://doi.org/10.1021/acs.est.5b04985, 2016.

McLinden, C. A., Adams, C. L. F., Fioletov, V., Griffin, D., Makar, P. A., Zhao, X., Kovachik, A., Dickson, N., Brown, C., Krotkov, N., Li, C., Theys, N., Hedelt, P., and Loyola, D. G.: Inconsistencies in sulfur dioxide emissions from the Canadian oil sands and potential implications, Environ. Res. Lett., 16, 014012, https://doi.org/10.1088/1748-9326/abcbbb, 2020.

O'Neill, N. T., Dubovik, O., and Eck, T. F.: Modified Ångström exponent for the characterization of submicrometer aerosols, Appl. Opt., AO, 40, 2368–2375, https://doi.org/10.1364/AO.40.002368, 2001.

O'Neill, N. T., Eck, T. F., Smirnov, A., Holben, B. N., and Thulasiraman, S.: Spectral discrimination of coarse and fine mode optical depth, J. Geophys. Res., 108, https://doi.org/10.1029/2002JD002975, 2003.

Park, J.-U., Park, J.-S., Diaz, D. S., Gebetsberger, M., Müller, M., Shalaby, L., Tiefengraber, M., Kim, H.-J., Park, S. S., Song, C.-K., and Kim, S.-W.: Spatiotemporal inhomogeneity of total column NO2 in a polluted urban area inferred from TROPOMI and Pandora intercomparisons, GIScience & Remote Sensing, 59, 354–373, https://doi.org/10.1080/15481603.2022.2026640, 2022.

Richter, A., Weber, M., Burrows, J. P., Lambert, J.-C., and Gijsel, A. van: Validation strategy for satellite observations of tropospheric reactive gases, Ann. Geophys., 56, https://doi.org/10.4401/ag-6335, 2013.

Simpson, I. J., Blake, N. J., Barletta, B., Diskin, G. S., Fuelberg, H. E., Gorham, K., Huey, L. G., Meinardi, S., Rowland, F. S., Vay, S. A., Weinheimer, A. J., Yang, M., and Blake, D. R.: Characterization of trace gases measured over Alberta oil sands mining operations: 76 speciated C_2–C_{10} volatile organic compounds (VOCs), CO_2, CH_4, CO, NO, NO_2, NO_y, O_3 and SO_2, Atmos. Chem. Phys., 10, 11931–11954, https://doi.org/10.5194/acp-10-11931-2010, 2010.

Sioris, C. E., Abboud, I., Fioletov, V. E., and McLinden, C. A.: AEROCAN, the Canadian sub-network of AERONET: Aerosol monitoring and air quality applications, Atmos. Environ., 167, 444–457, https://doi.org/10.1016/j.atmosenv.2017.08.044, 2017.

Song, H. and Yang, M.: Analysis on Effectiveness of SO_2 Emission Reduction in Shanxi, China by Satellite Remote Sensing, Atmosphere, 5, 830–846, https://doi.org/10.3390/atmos5040830, 2014.

Stieb, D. M., Burnett, R. T., Smith-Doiron, M., Brion, O., Shin, H. H., and Economou, V.: A New Multipollutant, No-Threshold Air Quality Health Index Based on Short-Term Associations Observed in Daily Time-Series Analyses, J. Air Waste Manag. Assoc., 58, 435–450, https://doi.org/10.3155/1047-3289.58.3.435, 2008.

Strawbridge, K. B.: Developing a portable, autonomous aerosol backscatter lidar for network or remote operations, Atmos. Meas. Tech., 6, 801–816, https://doi.org/10.5194/amt-6-801-2013, 2013.

Strawbridge, K. B. and Snyder, B. J.: Planetary boundary layer height determination during Pacific 2001 using the advantage of a scanning lidar instrument, Atmos. Environ., 38, 5861–5871, https://doi.org/10.1016/j.atmosenv.2003.10.065, 2004.

Strawbridge, K. B., Travis, M. S., Firanski, B. J., Brook, J. R., Staebler, R., and Leblanc, T.: A fully autonomous ozone, aerosol and nighttime water vapor lidar: a synergistic approach to profiling the atmosphere in the Canadian oil sands region, Atmos. Meas. Tech., 11, 6735–6759, https://doi.org/10.5194/amt-11-6735-2018, 2018.

Streets, D. G., Canty, T., Carmichael, G. R., de Foy, B., Dickerson, R. R., Duncan, B. N., Edwards, D. P., Haynes, J. A., Henze, D. K., Houyoux, M. R., Jacob, D. J., Krotkov, N. A., Lamsal, L. N., Liu, Y., Lu, Z., Martin, R. V., Pfister, G. G., Pinder, R. W., Salawitch, R. J., and Wecht, K. J.: Emissions estimation from satellite retrievals: A review of current capability, Atmos. Environ., 77, 1011–1042, https://doi.org/10.1016/j.atmosenv.2013.05.051, 2013.

5 Szykman, J., Swap, R. J., Lefer, B., Valin, L., Lee, S. C., Fioletov, V., Zhao, X., Davies, J., Williams, D., Abuhassan, N., Shalaby, L., Cede, A., Tiefengraber, M., Mueller, M., Kotsakis, A., Santos, F., and Robinson, J.: Connecting in-situ and Satellite Monitoring in Support of the Canada– U.S. Air Quality Agreement, EM: Air and Waste Management Association's Magazine for Environmental Managers, 7, 2019.

Tzortziou, M., Herman, J. R., Cede, A., and Abuhassan, N.: High precision, absolute total column ozone measurements from
10 the Pandora spectrometer system: Comparisons with data from a Brewer double monochromator and Aura OMI, J. Geophys. Res., 117, D16303, https://doi.org/10.1029/2012JD017814, 2012.

Tzortziou, M., Herman, J. R., Cede, A., Loughner, C. P., Abuhassan, N., and Naik, S.: Spatial and temporal variability of ozone and nitrogen dioxide over a major urban estuarine ecosystem, J. Atmos. Chem., 72, 287–309, https://doi.org/10.1007/s10874-013-9255-8, 2015.

15 Tzortziou, M., Kwong, C. F., Goldberg, D., Schiferl, L., Commane, R., Abuhassan, N., Szykman, J. J., and Valin, L. C.: Declines and peaks in NO_2 pollution during the multiple waves of the COVID-19 pandemic in the New York metropolitan area, Atmos. Chem. Phys., 22, 2399–2417, https://doi.org/10.5194/acp-22-2399-2022, 2022.

Wang, S., Zhang, Q., Martin, R. V., Philip, S., Liu, F., Li, M., Jiang, X., and He, K.: Satellite measurements oversee China's sulfur dioxide emission reductions from coal-fired power plants, Environ. Res. Lett., 10, 114015, https://doi.org/10.1088/1748-
20 9326/10/11/114015, 2015.

Zhao, X., Fioletov, V., Cede, A., Davies, J., and Strong, K.: Accuracy, precision, and temperature dependence of Pandora total ozone measurements estimated from a comparison with the Brewer triad in Toronto, Atmos. Meas. Tech., 9, 5747–5761, https://doi.org/10.5194/amt-9-5747-2016, 2016.

Zhao, X., Griffin, D., Fioletov, V., McLinden, C., Davies, J., Ogyu, A., Lee, S. C., Lupu, A., Moran, M. D., Cede, A.,
25 Tiefengraber, M., and Müller, M.: Retrieval of total column and surface NO_2 from Pandora zenith-sky measurements, Atmos. Chem. Phys., 19, 10619–10642, https://doi.org/10.5194/acp-19-10619-2019, 2019.

Zhao, X., Griffin, D., Fioletov, V., McLinden, C., Cede, A., Tiefengraber, M., Müller, M., Bognar, K., Strong, K., Boersma, F., Eskes, H., Davies, J., Ogyu, A., and Lee, S. C.: Assessment of the quality of TROPOMI high-spatial-resolution NO_2 data products in the Greater Toronto Area, Atmos. Meas. Tech., 13, 2131–2159, https://doi.org/10.5194/amt-13-2131-2020, 2020.

30 Zhao, X., Fioletov, V., Alwarda, R., Su, Y., Griffin, D., Weaver, D., Strong, K., Cede, A., Hanisco, T., Tiefengraber, M., McLinden, C., Eskes, H., Davies, J., Ogyu, A., Sit, R., Abboud, I., and Lee, S. C.: Tropospheric and Surface Nitrogen Dioxide Changes in the Greater Toronto Area during the First Two Years of the COVID-19 Pandemic, Remote Sens., 14, 1625, https://doi.org/10.3390/rs14071625, 2022.

35

Appendix A.

Figure A1 shows WindRASS' successful sampling rate and number of successful observations as a function of altitude. The number of successfully observations was nearly complete below 200m, but decreased quickly from 200 m to 400 m (i.e., from about 80% to about 20%). Less than 5% of observed vertical wind profiles reach altitudes above 600 m.
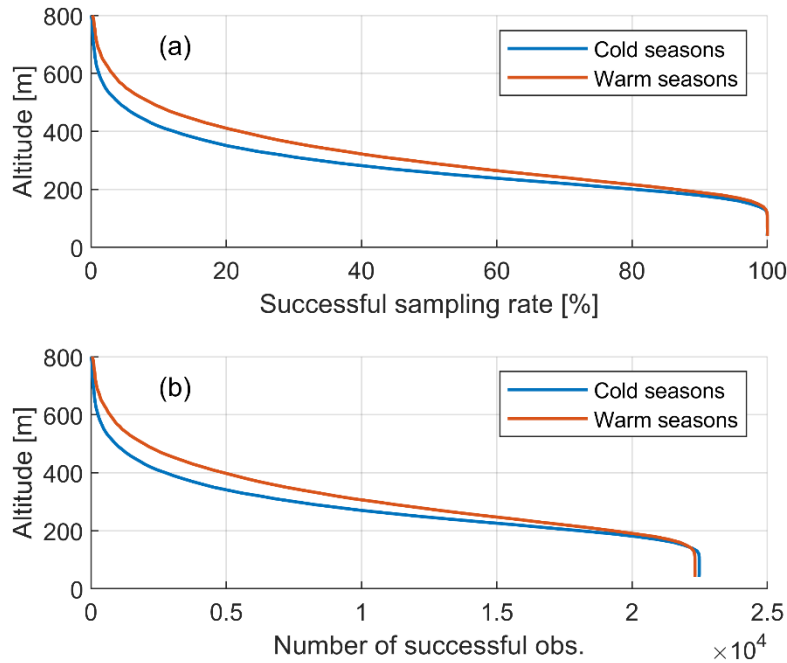
Figure A1. WindRASS successful sampling rate (recovery rate) and number of observations as a function of altitude.

~~Appendix B.~~

Appendix B.

SO₂ transport observations

Information about the wind speed in addition to wind direction could further help to characterize the pollution sources. In this section, the SO_2 observations from Pandora and in situ instrument are binned by the wind direction and speed data at a specific wind layer from WindRASS (i.e., SO_2 data binned by wind directions using 20° bins and by wind speed using 1 m s^{-1} bins, at a certain height). The SO_2 data are plotted using polar coordinates where the radius refers to the wind speed and angle refers to the wind direction. The color of the shading areas represents the VCD or surface concentration of SO_2. For example, Fig. B1a shows the Pandora SO_2 vertical column data displayed in such polar coordinates. The wind information for this plot

was from WindRASS data at a height of 250 m, as indicated on the plot. The wind layer was chosen as both the remote sensing and in situ observations show maximum sensitivity of the SO_2 plume at this layer (see Fig. 5). Figure 6a shows the pollutants (SO_2 VCD) were transported from 130° to 190° wind directions and reached maximum values at a wind speed of about 7 m s^{-1}. Low wind speed conditions (e.g., < 4 m s^{-1}) within this direction range will have lower observed signals compared to higher wind speeds. In contrast, Fig. B1b shows the in situ observations are sensitive to similar wind directions but elevated SO_2 surface concentrations are less sensitive to the wind speed than VCDs.
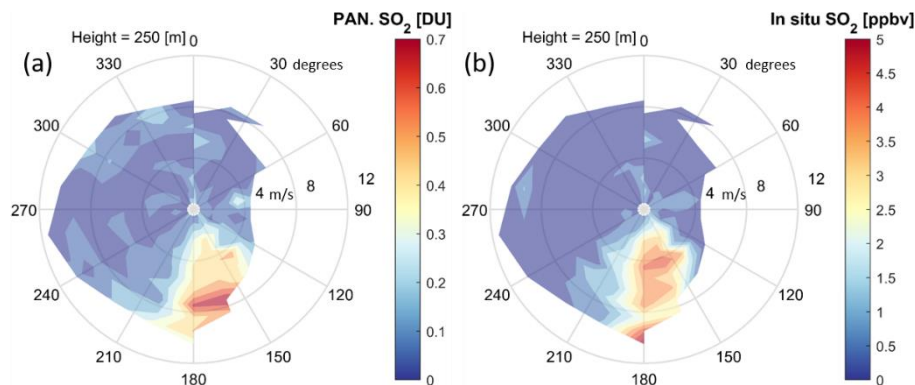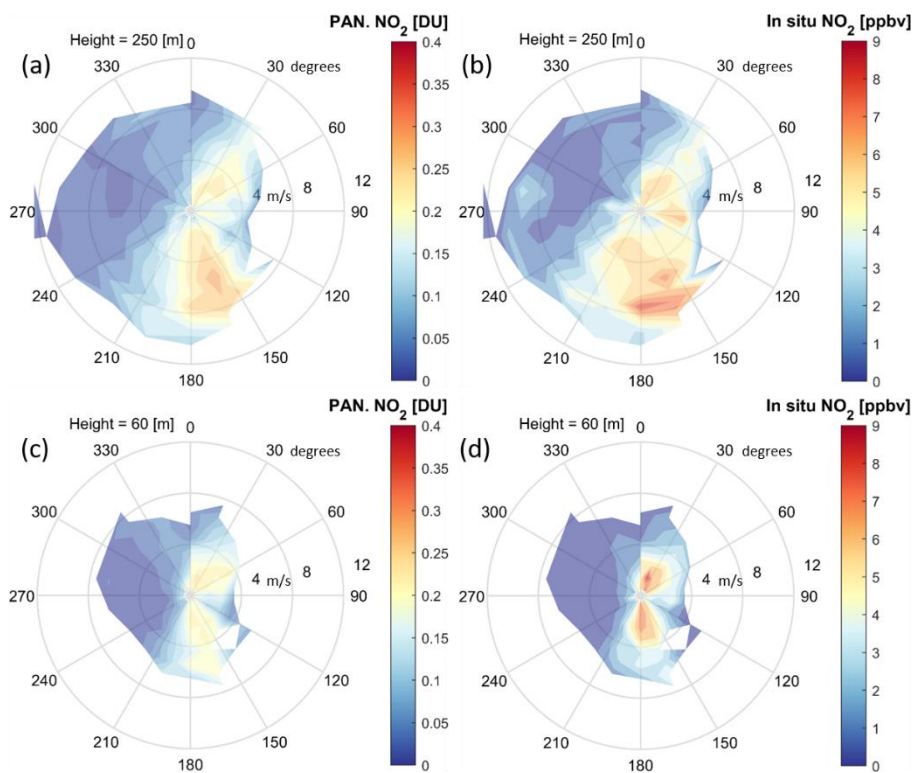

Figure B1. SO_2 horizontal transport pattern resolved by wind speed and directions. SO_2 observations from (a) Pandora (SO_2 VCD in DU) and (b) the in situ instrument (SO_2 surface concentration in ppbv) at Oski-Otin. Wind information from WindRASS data at 250 m layers where both Pandora and in situ instrument show maximum sensitivity to wind from the pollution sources (from 160°). The polar plot bins the SO_2 data (color-coded shading areas) by wind directions (angle values in degrees) and wind speed (radius values in m s^{-1}).

Both Pandora and in situ instruments show the same behaviour with wind speed: high SO_2 for relative higher wind speed (4–8 m s^{-1}) and low for low wind speed (<1 m s^{-1}). This is simply because there are no local SO_2 sources in Fort McKay. The higher the wind speed, the less time the pollutants need to travel from the source to the measurement site. Since the upgraders are about 20 km away from the observation site, fast winds would be corresponding to a transit time of about 1 hour; while slow winds would corresponding to about 6 hours. As SO_2 has a relatively short lifetimes in lower troposphere (of a few hours), the less time it takes to travel, the higher are the observed VCD or surface concentrations. If the wind speed is even higher (>8 m s^{-1}), the SO_2 signal is low again since the pollutant is spread over a larger area, while its total mass, determined by the emission rate and the lifetime, remains constant (e.g., see SO_2 VCD plume model from Fioletov et al., 2015).

NO$_2$ transport observations

For NO$_2$, the data were analyzed at two different wind layer heights, i.e., wind data from the 250 m layer (same as Fig. B1 which has high sensitivity to the wind direction for SO_2 data and remote sensing NO$_2$ data) and 60 m layer (high sensitivity for in situ NO$_2$ data, as shown in Fig. 6). In contrast to the single source direction for SO_2 (160°), two distinct NO$_2$ source directions were found at 40° and 160° (Fig. 6a and 6c). As shown in Fig. 1, the NO$_2$ source from 40° is related to the mining

43

area in the North West direction of the observation site (NO$_2$ emission mainly from mining fleet). The 160° directions have NO$_2$ emissions from both stacks and mining fleet (surface emissions >50%). The in situ instrument revealed the same source directions, but with different sensitivities to wind speed and wind layers. Fig. B2b shows that the 250 m layer wind is not good enough to isolate NO$_2$ sources, if using the in situ NO$_2$ observations. When using the wind layer at 60 m, Fig. B2d shows that the in situ instrument has increased sensitivity to surface NO$_2$ at low wind speed conditions (i.e., < 4 m s^{-1}). The results confirmed that remote sensing and in situ instruments have different sensitivity to different layers of the pollutants, thus when comparing the results of their observations, extra caution should be given to account for such differences. Note that the directions of the winds with the highest NO$_2$ values are somewhat different between the two layers that may be related to vertical wind shear.

Figure B2. NO$_2$ horizontal transport pattern resolved by wind speed and directions. NO$_2$ observations from (a, c) Pandora (NO$_2$ VCD in DU) and (b, d) in situ instruments (NO$_2$ surface concentration in ppbv) at Oski-Otin. Wind information from WindRASS data at 250 m layer (a and b) and 60 m layer (c and d). The polar plot bins the NO$_2$ data (color-coded shading areas) by wind directions (angle values in degrees) and wind speed (radius values in m s^{-1}).

Aerosol transport observations

As illustrated in Fig. 7 and discussed in Sect. 4.3, there are larger differences between AOD and in situ measurements in determining the aerosol pollution directions. It is worth noting that there were no clear vertical structures that can be used to

44

identify the optimal wind layers to separate and isolate potential aerosol sources. As a result, various wind layers and wind bins were examined. Not surprisingly, we did not find an optimal wind layer or wind bins that shows agreement between remote sensing and in situ measurements (see Fig. B3; which shows only warm seasons, when the aerosol loads are high). However, some general patterns can still be observed. In situ data show a clear aerosol source at 160° and other sources from the North and North East (see Fig. B3b and B3d; 250 m and 60 m wind layers, respectively), but with slightly different patterns in terms of wind speed. The source in the North-East directions can be detected in high wind conditions (e.g., about 7 m s^{-1}), whereas the source in South East directions can be detected in almost all wind conditions. This could indicate different distances of the source of PM$_{2.5}$ and the observation site, i.e., the South East source is closer. It is also worth noting that remote sensing instruments revealed those two aerosol sources, e.g., Fig 8a. However, the remote sensing observations demonstrate elevated AODs only for high wind conditions. A better explanation of such difference between sunphotometer's fine mode AOD and in situ instrument's PM$_{2.5}$ observations is still needed.
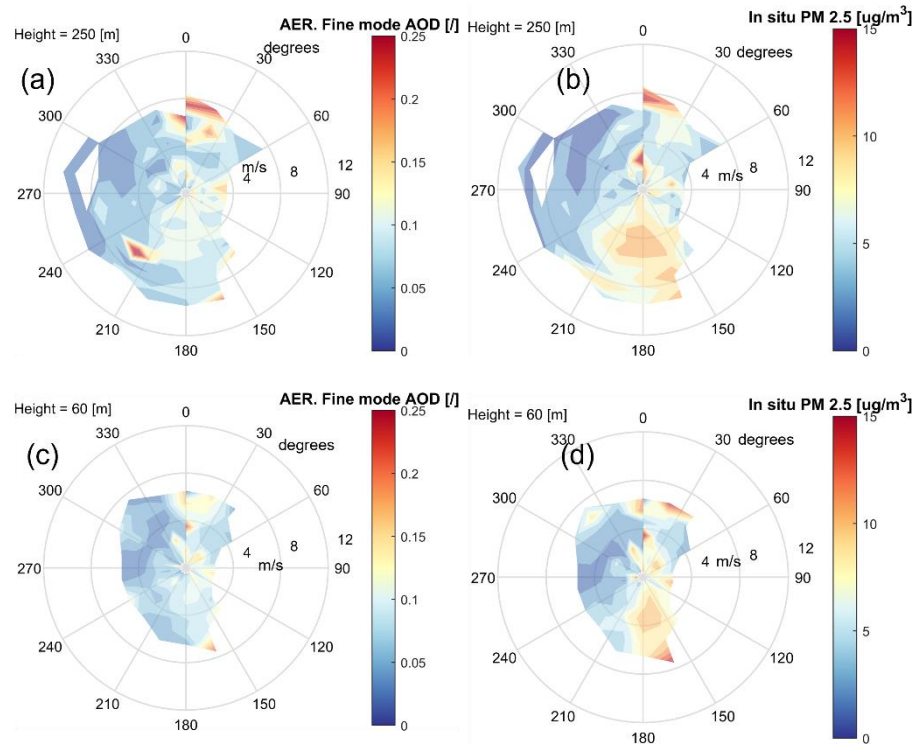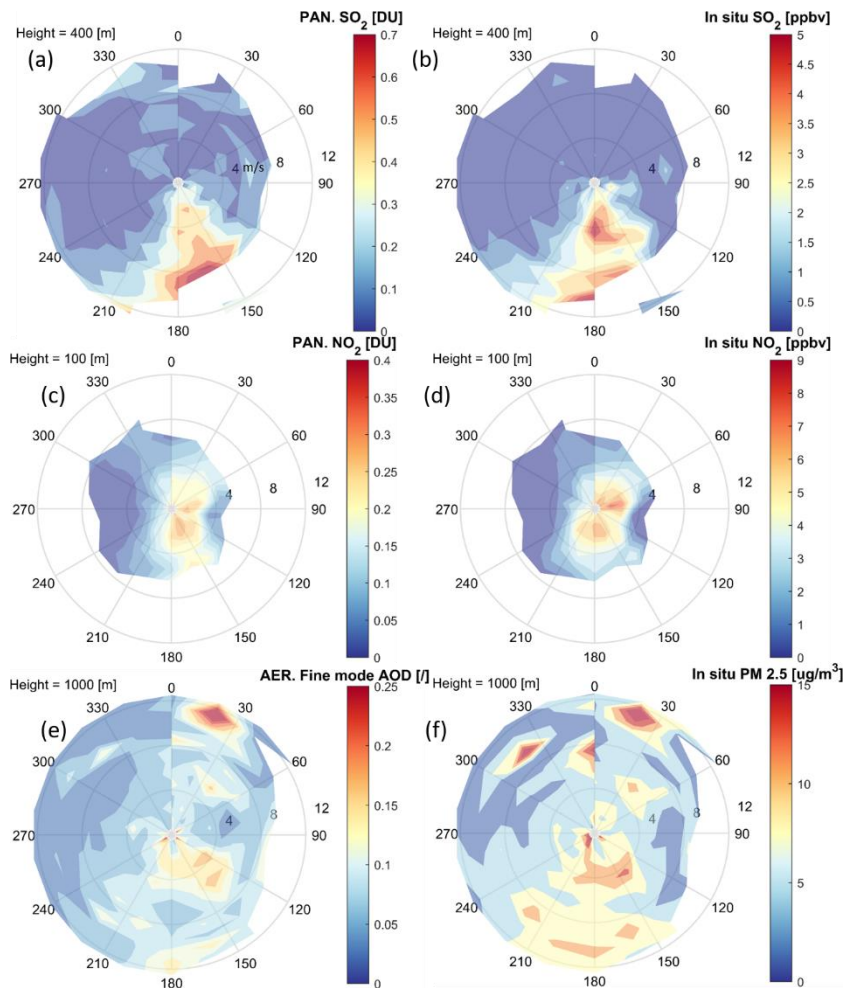
Figure B3. Aerosol horizontal transport pattern resolved by wind speed and directions. Aerosol observations from (a and c) sunphotometer (fine mode aerosol optical depth, unitless) and (b and d) the in situ instrument (PM$_{2.5}$ surface concentration in µg m^{-3}) at Oski-Otin. Wind information from WindRASS data at 250 m layer (a and b) and 60 m layer (c and d). The polar plot bins the aerosol data (color-coded shading areas) by wind directions (angle values in degrees) and wind speed (radius values in m s^{-1}).

Appendix C.

With the ERA-5 wind data, horizontal transport patterns were also ~~analysed~~ analyzed for SO$_2$, NO$_2$, and aerosol observations. ~~The results are consistent with the results of Sect. 4.~~ For example, Figs. ~~B1a~~ C1a and b confirmed that Pandora SO$_2$ column data is more sensitive to high wind speed conditions than in situ surface SO$_2$ data. Similarly, Figs. B1c and d identified two NO$_2$ sources from expected directions. Also, Fig. ~~B1d~~ C1d is consistent with Fig. ~~7d~~B2d, both show the in situ NO$_2$ data is more sensitive in low wind conditions. It is worth noting that, for the aerosol data, the AOD sources can be better identified and separated (see the discussion in Sect. 5.1) for higher-level winds (1000 m). In general, it was found that the optimized ERA-5 wind layers for NO$_2$ pollutants transport analysis in this region range from the surface to 900 hPa year-round (corresponding to the bottom 15 layers in ERA-5 model level data). As the SO$_2$ emissions were from high stacks, in warm seasons, its optimized wind layers extended from the surface to 800 hPa (corresponding to the bottom 25 model layers); while in cold seasons, the optimized wind layers extended from the surface to only 900 hPa (the bottom 15 model layers).

46

With ERA-5 wind and BLH data, the boundary layer height effect shown in Sect. 5.2 has been reproduced in Figs. B2 and B3 for warm and cold seasons, respectively.

Figure ~~B1~~C1. SO₂, NO₂, and aerosol horizontal transport patterns were resolved by wind speed and directions with using ERA-5 wind data. Panels a, c, and e show the SO₂, NO₂, and aerosol column observations from Pandora and sunphotometer (fine mode aerosol optical depth, unitless); panels b, d, and f show the in situ observations at Oski-Otin. Wind information from ERA-5 data at 400 m layers (a and b), 100 m layer (c and d), and 1000 m layer (e and f). The polar plot bins the observation data (color-coded shading areas) by wind directions (angle values in degrees) and wind speed (radius values in m s⁻¹).
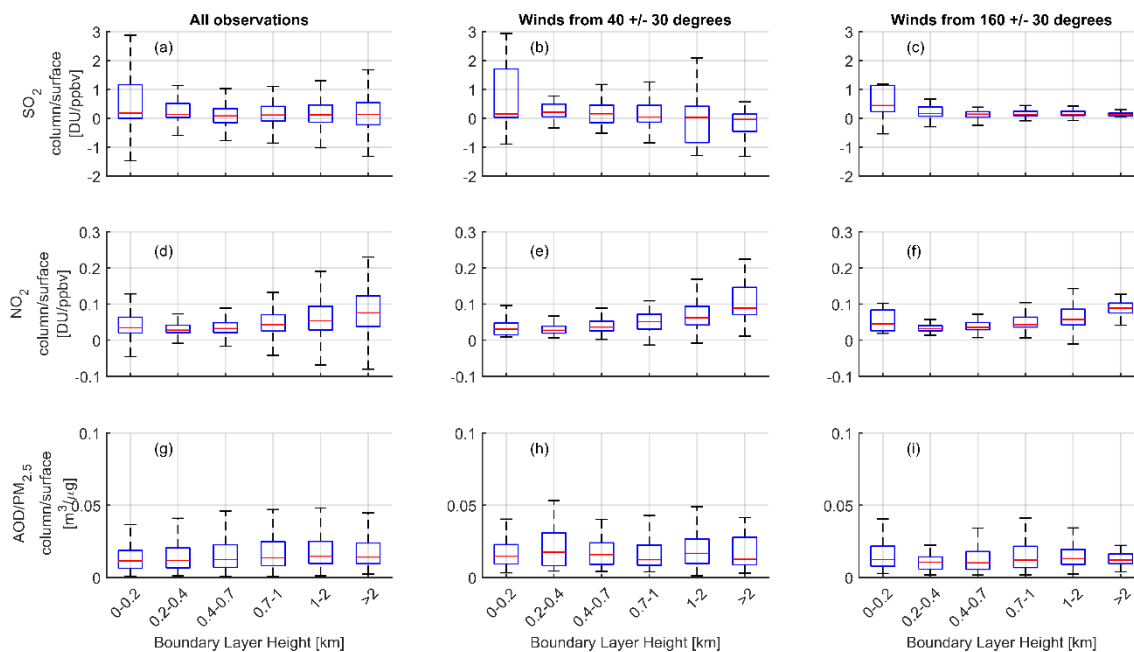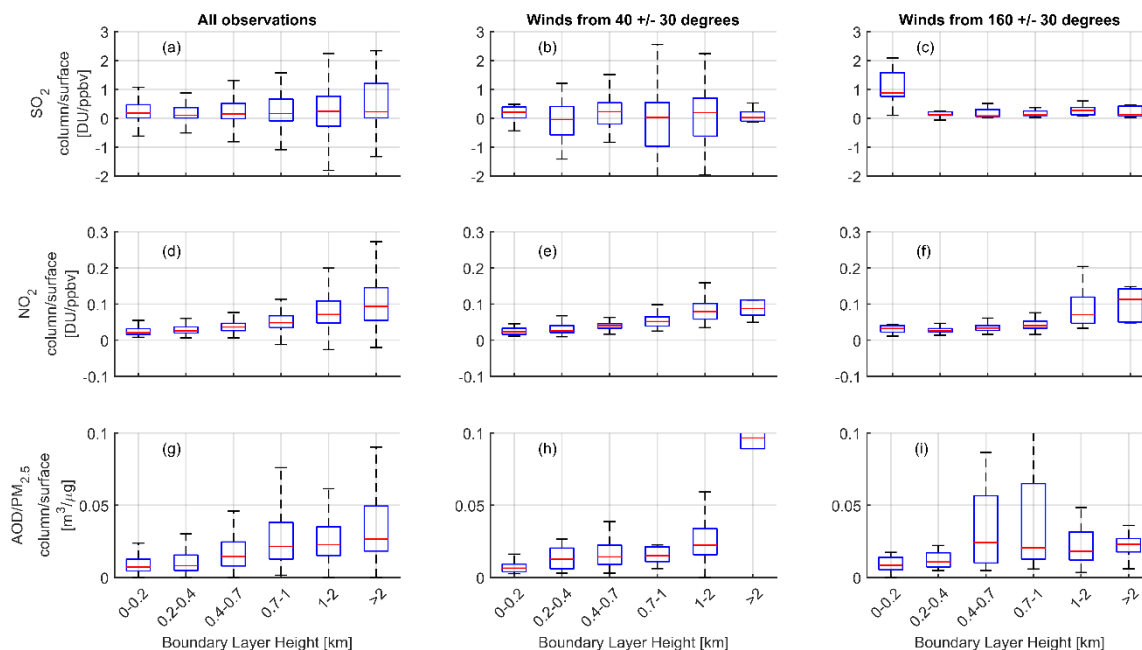
Figure B2C2. Boxplot of SO₂, NO₂, and AOD/PM₂.₅ column to surface ratio binned by boundary layer height in warm seasons. Panel (a), (d), and (g) show all observations; panels (b), (e), and (h) show observations with winds from 40° ± 30° directions; panels (c), (f), and (i) show observations with winds from 40° ± 30° directions. For SO₂ and AOD, the wind data is from ERA-5 at 300 m altitudes. For NO₂, the wind data is from ERA-5 at 100 m altitudes. The boundary layer height is from ERA-5. The SO₂ and NO₂ column observations are from Pandora, AOD observations are from sunphometer, and all surface concentrations are from in situ instrument.

Figure ~~B3~~C3. Boxplot of SO_2, NO_2, and $AOD/PM_{2.5}$ column to surface ratio binned by boundary layer height in cold seasons. Panel (a), (d), and (g) show all observations; panels (b), (e), and (h) show observations with winds from $40° \pm 30°$ directions; panels (c), (f), and (i) show observations with winds from $40° \pm 30°$ directions. For SO_2 and AOD, the wind data is from ERA-5 at 300 m altitudes. For NO_2, the wind data is from ERA-5 at 100 m altitudes. The boundary layer height is from ERA-5. The SO_2 and NO_2 column observations are from Pandora, AOD observations are from sunphometer, and all surface concentrations are from in situ instrument.

Table C1. Spearman correlation coefficients between median values of column to surface ratio and BLH height for Figure 10.

Panel	Fig. 10	Fig. 11	Fig. C2	Fig. C3
a	-0.49	0.37	-0.43	0.60
b	-0.09	-0.03	-0.83	-0.26
c	-0.83	-0.54	-0.94	-0.09
d	0.94	0.94	0.83	1.00
e	0.94	0.89	0.94	1.00
f	1.00	1.00	0.66	0.94
g	0.94	0.94	0.94	1.00

h	0.20	1.00	-0.31	1.00
i	0.49	0.66	0.26	0.60